Electrode improvement and neural network-based dynamic optimization of vanadium redox flow battery

Miss Apisada Chutimasakul

การปรับปรุงขั้วอิเล็กโทรดและการทำออพติไมเซชันแบบไดนามิกที่ใช้โครงข่ายนิวรัลของวานาเดียมรีดอกซ์โฟลว์แบตเตอรี่

น.ส.อภิษฎา ชุติมาสกุล

Thesis Title	Electrode improvement and neural network-based dynamic optimization of vanadium redox flow battery
By	Miss Apisada Chutimasakul
Field of Study	Chemical Engineering
Thesis Advisor	Assistant Professor Dr. AMORNCHAI ARPORNWICHANOP, D.Eng.

Accepted by the FACULTY OF ENGINEERING, Chulalongkorn University in Partial Fulfillment of the Requirement for the Master of Engineering

.... Dean of the FACULTY OF ENGINEERING

(Professor Dr. SUPOT TEACHAVORASINSKUN, D.Eng.)

THESIS COMMITTEE

.... Chairman

(Associate Professor Dr. SOORATHEP KHEAWHOM)

.... Thesis Advisor

(Assistant Professor Dr. AMORNCHAI ARPORNWICHANOP, D.Eng.)

.... Examiner

(Dr. Palang Bumroongsakulsawat, Ph.D.)

.... External Examiner

(Assistant Professor Dr. Yaneeporn Patcharavorachot, D.Eng., Ph.D.)

จุฬาลงกรณ์มหาวิทยาลัย

CHULALONGKORN UNIVERSITY

อภิษฎา ชุติมาสกุล : การปรับปรุงขั้วอิเล็กโทรดและการทำออพติไมเซชันแบบไดนามิกที่ใช้โครงข่ายนิวรัลของวา
นาเดียมรีดอกซ์โฟลว์แบตเตอรี่. (Electrode improvement and neural network-based
dynamic optimization of vanadium redox flow battery) อ.ที่ปรึกษาหลัก : ผศ. ดร.
อมรชัย อาภรณ์วิชานพ

ในงานวิจัยนี้ได้ทำการปรับปรุงประสิทธิภาพของแบตเตอรี่แบบมีการไหลของวานาเดียมที่เกิดปฏิกิริยารีดอกซ์ โดย
มีวัตถุประสงค์ 2 ประการ ได้แก่ 1) เพื่อวิเคราะห์ผลกระทบของอุณหภูมิของการบำบัดอิเล็กโทรดด้วยพลาสมาเจ็ทแบบความ
ดันบรรยากาศที่มีต่อประสิทธิภาพด้านพลังงานของแบตเตอรี่แบบมีการไหลของวานาเดียมที่เกิดปฏิกิริยารีดอกซ์ และ 2) เพื่อ
หาอัตราการไหลของอิเล็กโทรไลต์ที่เหมาะสมของแบตเตอรี่แบบมีการไหลของวานาเดียมที่เกิดปฏิกิริยารีดอกซ์โดยการทำออปติ
ไมเซชันแบบพลวัตซึ่งมีโครงข่ายนิวรัลจำลองเป็นแบตเตอรี่ จากการทดลองพบว่า การบำบัดอิเล็กโทรดด้วยพลาสมาเจ็ทแบบ
ความดันบรรยากาศที่อุณหภูมิ 550 องศาเซลเซียสทำให้แบตเตอรี่มีประสิทธิภาพด้านพลังงานสูงที่สุด ซึ่งอธิบายได้ด้วย
อุปกรณ์ตรวจจับสัญญาณเอกซเรย์ (EDX) และเทคนิคสเปกโตรสโกปีโฟโตอิเล็กตรอนด้วยรังสีเอ็กซ์ (XPS) อุปกรณ์
ตรวจจับสัญญาณเอกซเรย์แสดงให้เห็นว่าอิเล็กโทรดที่บำบัดด้วยพลาสมาเจ็ทแบบความดันบรรยากาศที่อุณหภูมิ 550 องศา
เซลเซียสมีอัตราส่วนร้อยละของอะตอมของออกซิเจนสูง และผลของการตรวจวัดด้วยเทคนิคสเปกโตรสโกปีโฟโตอิเล็กตรอน
ด้วยรังสีเอ็กซ์แสดงให้เห็นว่าอิเล็กโทรดที่บำบัดด้วยพลาสมาเจ็ทแบบความดันบรรยากาศที่อุณหภูมิ 550 องศาเซลเซียสมี
อัตราส่วนร้อยละของ $C=O$ สูงกว่าอิเล็กโทรดที่บำบัดด้วยพลาสมาเจ็ทแบบความดันบรรยากาศที่อุณหภูมิอื่นๆและการบำบัด
ด้วยกรดซัลฟูริก นอกจากนี้ความสามารถในการซึมผ่านของอิเล็กโทรดที่บำบัดด้วยพลาสมาเจ็ทแบบความดันบรรยากาศที่ทุก
อุณหภูมิจะปรับปรุงประสิทธิภาพของแบตเตอรี่ได้ดีกว่าอิเล็กโทรดที่บำบัดด้วยกรดซัลฟูริกและที่ไม่ผ่านการบำบัด อย่างไรก็
ตามการบำบัดอิเล็กโทรดไม่ส่งผลต่อพื้นผิวของอิเล็กโทรดซึ่งแสดงด้วยกล้องจุลทรรศน์อิเล็กตรอนแบบส่องกราด (SEM)
ในส่วนที่สองของการวิจัยได้ทำการหาอัตราการไหลที่เหมาะสมโดยใช้แบบจำลองโครงข่ายนิวรัลของแบตเตอรี่แบบมีการไหล
ของวานาเดียมที่เกิดปฏิกิริยารีดอกซ์ โครงข่ายนิวรัลถูกฝึกอบรมแบบแยกเป็นกระบวนการชาร์จและกระบวนการคายประจุโดย
ใช้แบบจำลองอนุกรมเวลาฟังก์ชั่นเป็นแบบไม่เชิงเส้น (NARX) ผลการฝึกอบรมและการทดสอบแสดงว่าแบบจำลอง
โครงข่ายนิวรัลมีความถูกต้องสูง โดยอัตราการไหลที่เหมาะสมจะได้มาจากการแก้ปัญหาออปติไมเซชัน โดยมีโครงข่ายนิวรัลเป็น
แบบจำลองของแบตเตอรี่แบบมีการไหลของวานาเดียมที่เกิดปฏิกิริยารีดอกซ์ ซึ่งให้ประสิทธิภาพของระบบสูงเนื่องจากการ
สูญเสียที่เกี่ยวเนื่องกับการถ่ายโอนมวลสารของสารวานาเดียมลดลง แสดงถึงแบบจำลองโครงข่ายนิวรัลสามารถใช้แทน
แบบจำลองเชิงทฤษฎีที่ใช้ในการทำออปติไมเซชันแบบพลวัต แม้ว่าประสิทธิภาพของแบตเตอรี่แบบมีการไหลของวานาเดียมที่
เกิดปฏิกิริยารีดอกซ์ภายใต้อัตราการไหลที่เหมาะสมที่ได้จากการทำออปติไมเซชันที่มีโครงข่ายนิวรัลเป็นแบบจำลองน้อยกว่าการ
ทำออปติไมเซชันที่มีแบบจำลองเชิงทฤษฎีเล็กน้อย

6070371021 : MAJOR CHEMICAL ENGINEERING

KEYWOR
D:
Vanadium redox flow battery, Dynamic optimization based on Neural Network, Neural Network, Electrode treatment, Atmospheric Pressure Plasma jets

Apisada Chutimasakul : Electrode improvement and neural network-based dynamic optimization of vanadium redox flow battery. Advisor: Asst. Prof. Dr. AMORNCHAI ARPORNWICHANOP, D.Eng.

The performance improvement of a vanadium redox flow battery (VRFB) was focused on this study. The two objectives of this study were (1) to investigate the effect of the operating temperatures of the Atmospheric Pressure Plasma jets (APPJs) process on the energy efficiency of the VRFB and (2) to determine the optimal electrolyte flow rate of the VRFB by solving a dynamic optimization based on a neural network model of the VRFB. The APPJs graphite felt electrode treatment temperature providing the highest energy efficiency of the VRFB was 550°C, explained by the Energy Dispersive X-ray Spectrometry (EDX) and X-ray photoelectron spectroscopy (XPS) results. The EDX results indicated that the electrode treated with APPJs at 550°C had a high percentage of the oxygen atom, and XPS results illustrated the highest C=O functional group on the surface of APPJs at 550°C electrode comparing to the APPJs at other temperatures and sulfuric treatment. Moreover, the wettability of the electrode with APPJs treatment at all temperatures was higher improved than that with a sulfuric acid treatment and an untreated one. However, the electrode treatment did not visibly change the surface of the electrode, as shown in Scanning Electron Microscopy (SEM) results. In the second part of this study, an optimization of the electrolyte flow rate based on a neural network (NN) model of the VRFB was investigated. The NN was separately trained between the charging and discharging process using a nonlinear autoregressive with external input (NARX) model. The training and testing results indicated a high accuracy of the NN model. Under the optimal electrolyte flow rate obtained by solving the NN based-optimization, the VRFB provided a high system efficiency (SE) due to reducing the concentration overpotential. It demonstrated that the NN model could replace the theoretical model used in the dynamic optimization, even though the performance of the VRFB under the optimal electrolyte flow rate obtained from the NN-based optimization is slightly lower than that from the theoretical model-based optimization.

Field of Study:	Chemical Engineering	Student's Signature ....
Academic Year:	2020	Advisor's Signature ....

ACKNOWLEDGEMENTS

TABLE OF CONTENTS

LIST OF FIGURES

จุฬาลงกรณ์มหาวิทยาลัย

CHULALONGKORN UNIVERSITY

LIST OF TABLES

จุฬาลงกรณ์มหาวิทยาลัย

CHULALONGKORN UNIVERSITY

CHAPTER 1

INTRODUCTION

1.1   Background

Conventional electricity production is based on the combustion of fossil fuels that releases CO_2 to the environment and causes a global warming problem. Due to environmental concerns, the use of renewable energy plays an important role in the generation of electricity. However, renewable energy is intermittent and discontinue. Energy storage can be used to solve this major problem, stabilizing a power output. Among the various types of energy storages, a vanadium redox flow battery (VRFB) is considered to be the most suitable for large-scale energy storage due to its high efficiency and low cost per kilowatt (Zhao et al., 2017). The advantages of the VRFB include its high flexibility, long-life cycle, and tolerance for deep discharge. In principle, the VRFB stores electrical energy via redox reactions in the electrolyte solution, which is circulated through the electrode by a pump and kept outside the battery. By contrast, other types of batteries, such as Lithium-ion batteries, store energy inside electrodes that involve the ion transfer. Therefore, the power rating of a VRFB can be obtained from the number of battery cells and the capacity is determined by the electrolyte volume and redox-active chemical species concentrations. However, the main problem of VRFB is caused by the imbalance of redox species in catholyte and anolyte, that results in the decrease of battery efficiency.

To date, many researchers have developed various components of the VRFB, including the electrolyte solution (Nguyen et al., 2016), types of the membrane (Bengui et al., 2018), flow field pattern (Kumar & Jayanti, 2016), and electrode material (Kabtamu et al., 2018), to increase battery performance. Since the redox reactions occur at the surface of the electrode, the development of the electrode is a key factor to improve battery performance. The electrode performance can be improved via an electrode treatment processing such as heat treatment, acid treatment, and plasma treatment. Acid treatment is a widely used method for the graphite felt

electrode in the VRFB system. Xiao-gang et al. (2007) studied the efficiency of the VRFB using the electrode with an acid treatment and found battery efficiency enhancement. Dixon et al. (2016) also reported that battery performance increased when the electrode treated with heat and plasma was used. These two treatment methods did not increase the surface area and there was no weight loss. However, the VRFB with plasma treatment showed better efficiency than that with heat treatment due to less charging time and capacity loss. Moreover, the electrode treated with atmospheric pressure plasma jets (APPJs) studied by Chen et al. (2015). They showed the energy efficiency improved from 70% (untreated) to 82% (treated with APPJs) as the increased C-O and C=O functional groups. However, the optimal temperature of the APPJs process that provides higher efficiency of the electrode was not reported.

Atmospheric pressure plasma jets are generally operated under atmospheric pressure. Plasma technology is a clean technology because of using less water and chemicals. The jet allows for the generation of stable plasmas, thus the APPJs are applied to several fields such as biomaterial sterilization and treatment (Bartis et al., 2013), coating thin film (Hossain et al., 2019), rapid sintering of nanoporous TiO_2 (Chang et al., 2014; Chang et al., 2013), surface modification and cleaning (Chiang et al., 2010; Homola et al., 2012), and electrode treatment (Chen et al., 2015).

Since the vanadium redox flow battery (VRFB) is a type of flow battery, the electrolyte flow rate is key to the process. It affects the stack and electrolyte temperature as the flow rate reduction causes the stack and electrolyte temperature to increase(Tang et al., 2012). The electron transfer coefficient is increased by increasing the electrolyte flow rate and temperature (Kim & Park, 2019). Although, the high electrolyte flow rate is good with some parameters, the too high flow rate may have some disadvantages, such as high pump energy consumption. Therefore, the electrolyte flow rate should be optimized to provide high battery efficiency. Tang et al. (2014) studied battery performance under constant and variable electrolyte flow rates. The variable flow rate of the electrolyte can more improve the trend of coulombic efficiency, energy efficiency, discharge capacity, and system efficiency than using the constant flow rate strategy. The high flow factor could improve the VRFB performance due to a decrease in the concentration overpotential; however,

using the higher electrolyte flow rate will increase the large power loss of the pump that affects the system efficiency. Jirabovornwisut et al. (2020) studied the electrolyte flow rate optimization with minimizing charging energy and maximizing discharging energy by the nonlinear programming optimization. The flow rate nonlinear programming optimization showed the enhanced system efficiency than the variable flow rate because the variable flow rate required more cycle time and the battery voltage sharply increased and decreased in the early and middle stages affect to battery power. Accordingly, an optimization process is a suitable method for enhancing the system efficiency of the vanadium redox flow battery.

Neural network (NN) is artificial intelligence (AI) that works like the human brain neuron, based on training, remembering, and analyzing in the way that it had trained. Because the neural network can effectively solve complex mathematical models and get more accurate and precise answers. The neural network recently plays an important role in predicting various situations and applying to a wide range of applications such as agriculture (Saengsawang, 2016), geography, economics (Grekousis, 2019), and energy and technology (Ruiz et al., 2019; Wu et al., 2018). Even though the mathematical model is absent. The NN is considered as a black block model can be trained with experimental results. The backpropagation neural network model was used to predict the stack voltage and current of the commercial proton exchange membrane (PEM) fuel cell system using the laboratory data for training in the research of Saengrung et al. (2007). The battery temperature also is an important parameter in battery life degradation, safety, and performance. Hasan et al. (2020) estimated the battery temperature by using the Non-linear Autoregressive Exogenous (NARX) neural network that collecting each seasonable temperature data as a training data set and this model shown the better performance compared to the universal model. There are many other studies using NN in the battery field; however, there is a little amount of research that uses a NN to estimate parameters for the operation of vanadium redox flow batteries.

In this study, the effect of operating temperatures of the APPJs process on the VRFB energy efficiency is investigated. Furthermore, a comparison of the VRFB performance using sulfuric and APPJs electrode treatments is made. The surface

morphology of the graphite felt electrode with un-treated, acid treatment, and APPJs treatment is reported. Besides, an optimal flow rate of the VRFB electrolyte determined by using a neural network is focused on this work.

1.2   Objective

1.2.1 To investigate the effect of the operating temperatures of the APPJs process on the energy efficiency of the VRFB.

1.2.2 To determine the optimal electrolyte flow rate of the VRFB by solving a dynamic optimization based on a neural network model.

1.3   Scope of research

1.3.1 Prepare electrodes treated with APPJs at different temperatures (450°C, 550°C, and 650°C) and conventional sulfuric acid (H_2SO_4).

1.3.2 Characterize the treated electrodes using Scanning Electron Microscopy (SEM) and X-ray photoelectron spectroscopy (XPS) to determine the surface morphology and the functional group on the surface.

1.3.3 Assembly the VRFB cell and determine the battery performance (the coulombic, voltage, energy efficiencies and discharge capacity) using the treated electrode. The lower and upper cut-off voltages are 0.7 and 1.71 V, respectively.

1.3.4 Develop the VRFB model for simulation and validate this model with the best experiment result.

1.3.5 Train, validate, and test the VRFB neural network model in which separating the charge and discharge model.

1.3.6 Formulate a dynamic optimization problem using the developed neural network model to determine an optimal electrolyte flow rate of the VRFB, providing minimize total charging power and maximize total discharging power.

CHAPTER 2

THEORY AND LITERATURE REVIEWS

2.1   Theory

2.1.1   Vanadium redox flow battery (VRFB)

VRFB is one of the energy storages for renewable energy. The prominent point of VRFB is the separation of power rating and capacity. The power rating can be determined by the number of cells stack and the battery capacity can determine by the electrolyte volume or the active vanadium species in the electrolyte. The electrolyte consists of the different oxidation states of vanadium ion which are V^{2+}/V^{3+} in a negative electrolyte (anolyte) and V^{4+}/V^{5+} (VO^{2+}/VO_2^+) in a positive electrolyte (catholyte). The reactions of VRFB occurred at the electrodes are follow as:

Positive half-cell:

$$VO^{2+} + H_2O \underset{discharge}{\overset{charge}{\rightleftarrows}} VO_2^+ + 2H^+ + e \qquad E_p^0 = 1.004 \text{ V.} \qquad (2.1)$$

Negative half-cell:

$$V^{3+} + e^- \underset{discharge}{\overset{charge}{\rightleftarrows}} V^{2+} \qquad E_n^0 = -0.255 \text{ V.} \qquad (2.2)$$
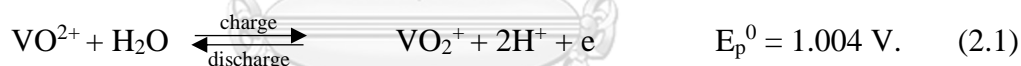
For the oxidation-reduction reactions in the charging process, V^{4+} (VO^{2+}) is converted to V^{5+} (VO_2^+) in the positive half-cell, and the electron will transfer to the negative half-cell by the external circuit, causing V^{3+} is converted to V^{2+}, respectively. Meanwhile, the proton or hydrogen ion (H^+) will diffuse across the membrane between the positive and negative half-cell. The discharging process alternates with the charging process that the V^{2+} is converted to V^{3+} by oxidation process and an electron transferred making V^{5+} (VO_2^+) convert to V^{4+} (VO^{2+}) in the reduction reaction occurring the negative and positive half-cell, respectively. Figure 2.1 shows the schematic and mechanism of VRFB.
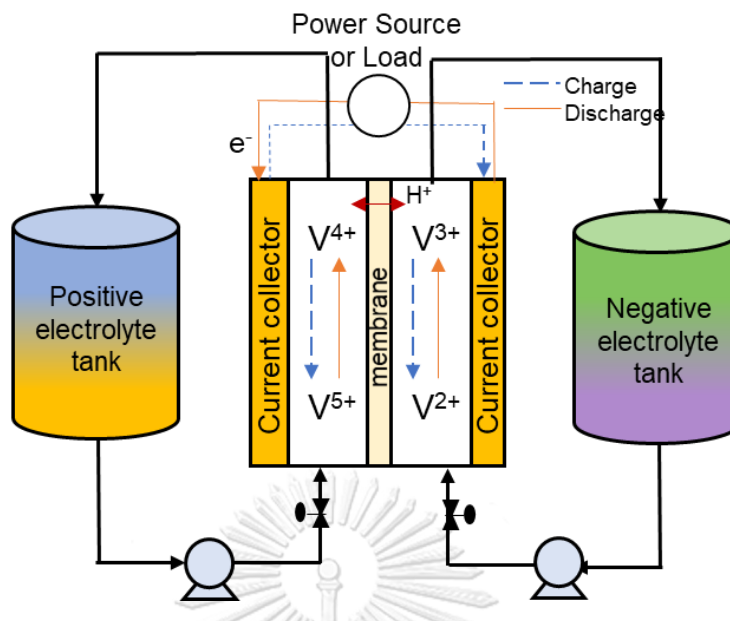
Figure 2.1 Schematic and mechanism of redox reaction in the VRFB system.

2.1.1.1   Overpotential

The overpotential is the difference between the open-circuit voltage (theoretical voltage) and the actual cell voltage. Consequently, the battery needs the more applied voltage to charge the battery, and less discharged voltage is provided by the battery. The overpotential contains three parts as activation overpotential, ohmic overpotential or ohmic loss, and concentration overpotential. The energy loss due to the slowness of the electrochemical reactions at the cathodic and anodic electrodes is called activation overpotential. It is a measure of the activity of electrodes and represents the energy required for the electrochemical reactions which is the activation energy of redox reactions. The ohmic loss is the electrical potential that compensates for the electrical resistance of each part of the cell. The concentration overpotential refers to the equilibrium potential difference across a diffusion layer given a particular electrode reaction and density. It is used to describe the distribution of the electrolyte in the cell occurring in the diffusion layers by mass diffusion process at the electrolyte/electrode interface. The concentration loss is affected by the electrolyte flow rate, particularly at high and low states of charge. When the active species concentration in the electrolyte is low, the mass transfer rate of the active

species ions to the electrode surface is unable to keep up with the transfer of electrons across the electrode/electrolyte interface.

2.1.2   Atmospheric pressure plasma jets (APPJs)

Plasma jet is a plasma generated by gas that is forced to flow through the nozzle electrode, which has an electric field and high frequency. The gas is formed into plasma and is pushed out by the gas pressure from the supply. A plasma with a diameter of 1-2 mm, called a plasma jet can operate at atmospheric pressure (APPJ) (Baral et al., 2012; Nehra et al.; Schutze et al., 1998). The APPJ can improve or modify the surface of many materials without affecting the material properties (Teschke et al., 2005). The atmospheric pressure plasma jet process illustrates in Figure 2.2.
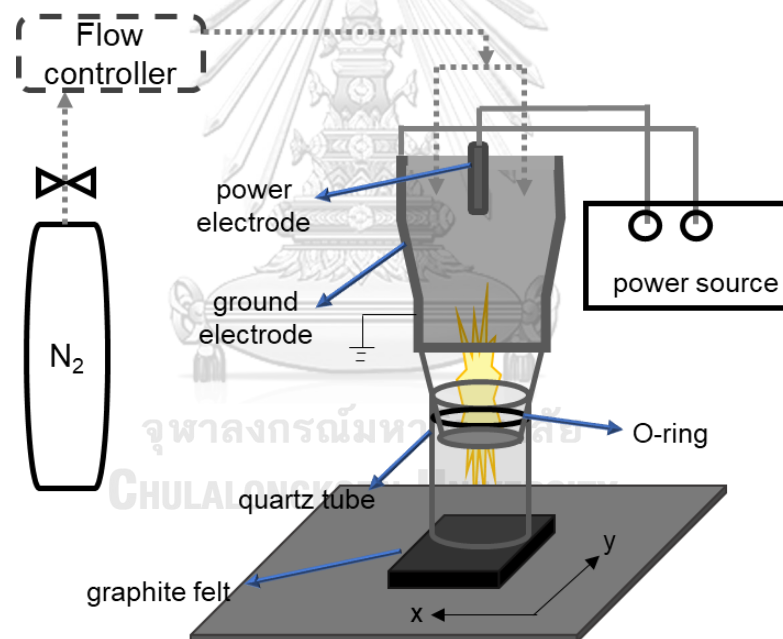
Figure 2.2 The atmospheric pressure plasma jet process.

2.1.3   Artificial Neural Network

Artificial Neuron Network (ANN) is a branch of artificial intelligence (AI), which has the same structure and function as the brain of an organism. It can respond to the input data according to the learning rule after the network has learned. The neural network has been imitated from the work of the human brain. The human brain can be called a computer that has self-adaptive, non-linear, and works parallel to

supervise the working management of neurons in the brain. The brain consists of a basic processor called a neuron. The human brain has many amounts of the neuron (about 10^{11}), and there are neural networks made up of three important parts: the dendrite, the cell body (soma) and the axon, as shown in Figure 2.3. Dendrite is the part of the neuron cell that extends around the cell. A neuron has many dendrite branches, which act as a nerve signal receptor to the cell body or soma. The cell body is the address of the nucleus and various cell organelle. It is responsible for synthesizing nerve signals and sending them to the axon. The axon is a nerve fiber that carries nerve signals from the cell body. One neuron will have only one axon, which is a longitudinal cell extension that acts as a nerve signal out of the cell (Wannaphong, 2016).
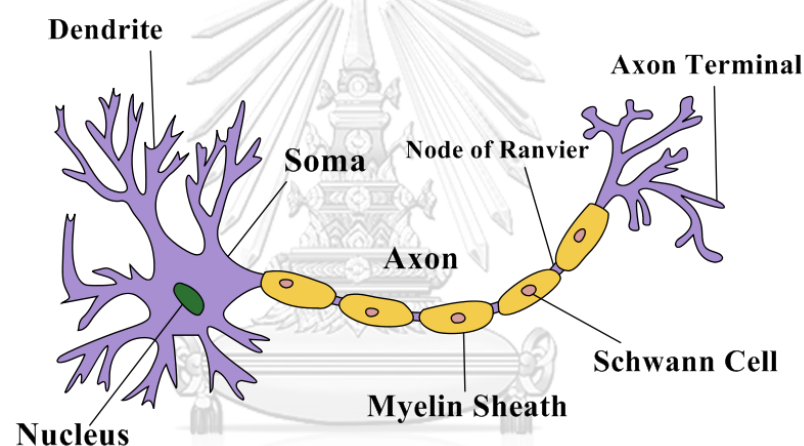
Figure 2.3 The structure of a neuron (Flagg, 2013).

Node is simulating the behavior of a neuron in the neural network. Within the node has a function to set the output signal called the transfer function, which acts as a process in the cell. Each network consists of nodes connected as layers, which have different functions. Figure 2.4 shows the neural network schematic. The neural network consists of 5 elements as follows (Techology, 2016):

1. Input data (x_i) is numeric data. If it is qualitative data, it must be converted into a quantitative form which is acceptable to the neural network.

2. Weights (w_i) are derived from the learning of artificial neural networks. Weights are an important component of the neural network system

identifying the relationship between the input data. The trial and error method is used to make the conclusion of each relationship and keep it as a pattern or pattern of experience for network learning.

3. Summation function (S) is responsible for combining the weight (w_i) and the input (x_i) to summarize the relationship between the input data, waiting for the conversion of information in the next layer as in Eq.2.3.

$$S = \sum_{i=1}^{n} p_i w_i \qquad (2.3)$$

4. Transfer function or activation function is the part that combines numerical values from the neural output and then decides whether to send the output signal in any form. The transfer function can be linear or nonlinear. The selection of the transfer function depends on the nature of the system that uses the neural network to apply. The transfer functions have many typical applications detailed in Table 2.1. The log-sigmoid transfer function is the most commonly used due to the continuous value of the output allowance.

5. Output data (y_i) is the actual result of the learning process of artificial neural networks.
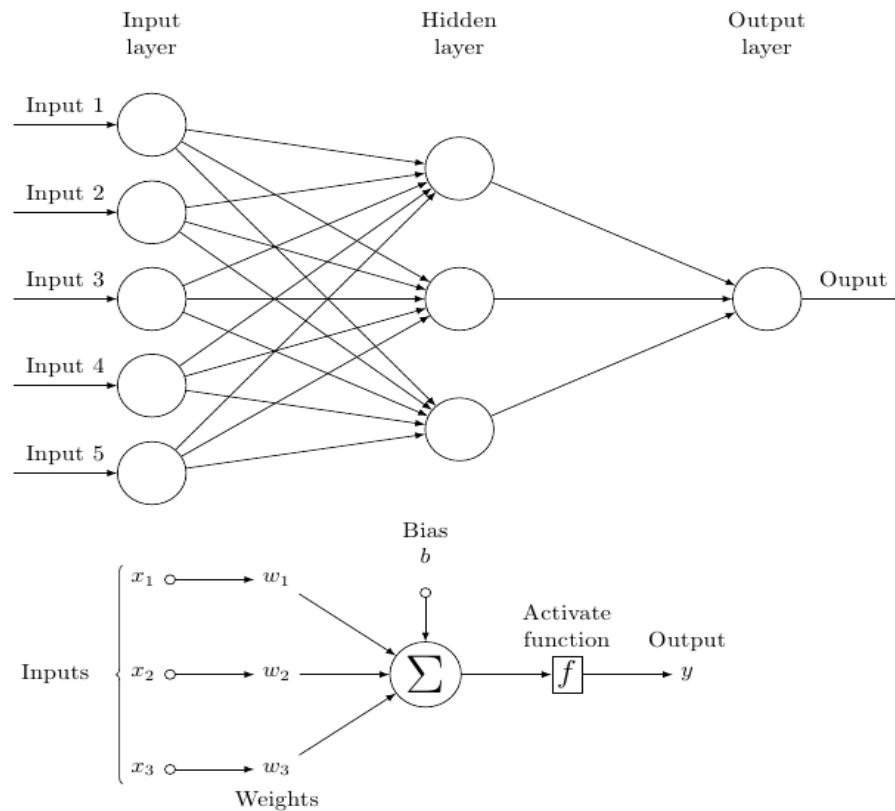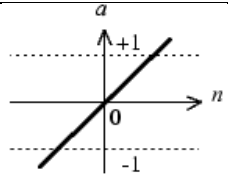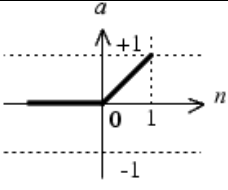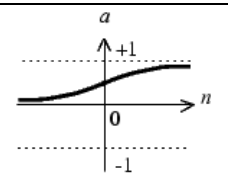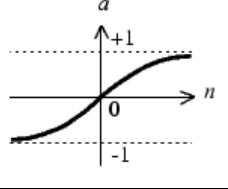
Figure 2.4 The artificial neural network schematic ("Diagram of an artificial neural network," 2013).

Table 2.1 The artificial neural network transfer functions (Techology, 2016).

Transfer function	Equation	MATLAB function	Function graph
Hard limit transfer function	$f(x) = \begin{cases} 1 \ if \ x \geq 0 \\ 0 \ if \ x < 0 \end{cases}$	hardlim	
Symmetrical hard limit transfer function	$f(x) = \begin{cases} 1 \ \ if \ x \geq 0 \\ -1 \ if \ x < 0 \end{cases}$	hardlims	

Linear transfer function	$f(x) = x$	purelin	
Positive linear transfer function	$f(x) = \begin{cases} 0 \ if \ x < 0 \\ x \ if \ x \geq 0 \end{cases}$	poslin	
Log-sigmoid transfer function	$f(x) = \dfrac{1}{1+e^{-x}}$	logsig	
Hyperbolic tangent sigmoid transfer function	$f(x) = \dfrac{e^x - e^{-x}}{e^x + e^{-x}}$	tansig	

2.1.3.1 Network architecture

Classification of artificial neural network structures according to the direction of motion of the signal can be divided into two categories: feedforward network and feedback network.

A feedforward network is an architecture that has data transmission only in one direction from the input to output, and the nodes in the same layer are not connected. A feedforward network consists of an input layer, hidden layers, and an output layer. A feedforward network can be divided into two types: single-layer and multilayer depend on a hidden layer, shown in Figure 2.5. The output of a neural network is an input of the same network is called a feedback network. A feedback structure appears in many applications; such as an optimization problem solver (Zhang, 2000).
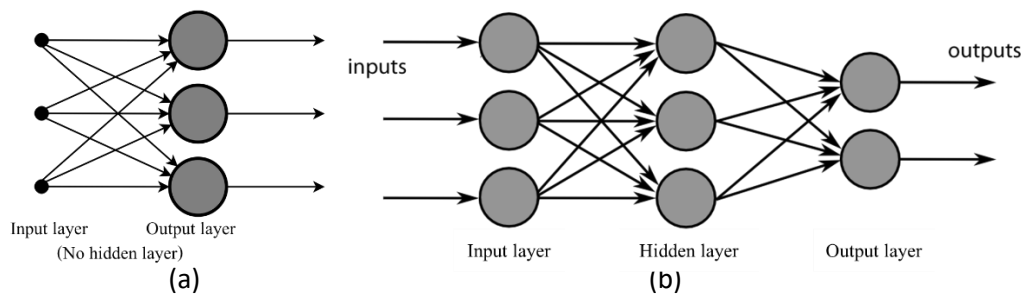
Figure 2.5 The feedforward network structure (a) single-layer network and (b) multilayer network with one hidden layer.

2.1.3.2   Backpropagation algorithm

The properties of artificial neural networks are the ability to learn from the samples by trying to calculate the relationship between inputs and results. This learning begins with the initial weight and deviation (bias). The results from the initial values are compared with actual results. Different values are used to adjust the weight and bias by the trial-and-error method until the results are close or match actual results. The final weight and bias values will be used to predict the results from the new data.

Backpropagation is a process commonly used to adjust the weight and bias, which consists of two signals: the function signals and the error signals. The function signals are the information or results of each unit sent to the network. The error signals or error function is the difference between the result of the calculation and the actual result that is returned to the neural network to adjust the weight and bias.

There are several methods for adjusting the weight and bias such as Gradient Descent, Descent with Gradient Descent with Rate, Gradient Descent with Momentum, Resilient, Bayesian Regularization, and Levenberg-Marquardt, etc. Levenberg-Marquardt (LMS) is a suitable training algorithm for troubleshooting estimation type problems. In addition, it is the fastest way to adjust the value (Demuth & Beale, 1992-2004).

2.1.3.3   Nonlinear Autoregressive Exogenous (NARX)

Nonlinear Autoregressive Exogenous (NARX) is a type of neural network that uses time series on external input data in the learning of the neural network which can feedback information that increases the learning accuracy of the neural network. NARX networks can learn to predict one time series from given past values of the same time series, the feedback input, and another time series to predict future data precisely. The NARX model is usually used in nonlinear dynamic systems (The MathWorks, 2020). An example of NARX model diagram is shown in Figure 2.6.
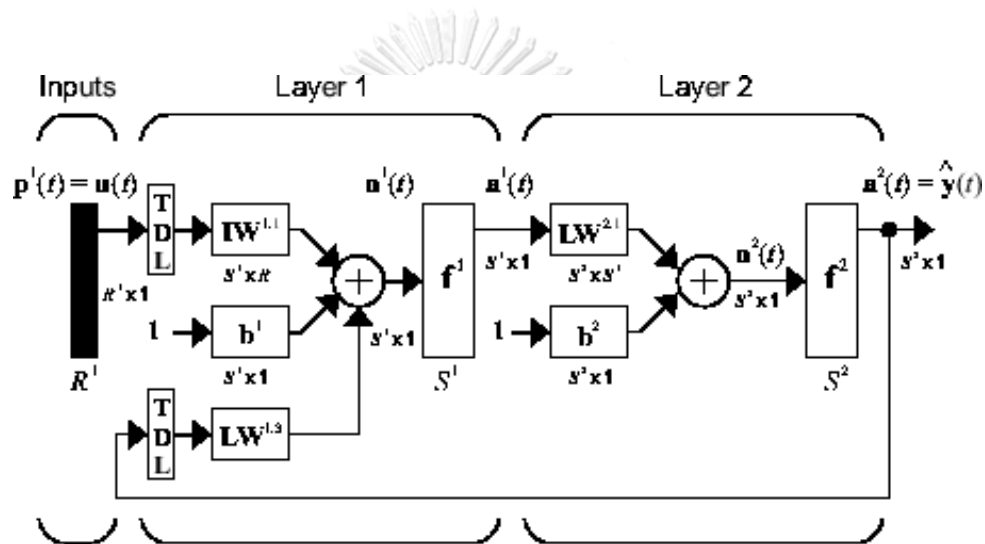
Figure 2.6 An example of NARX model diagram (The MathWorks, 2020).

2.1.4   Optimization

Optimization is a mathematical process that results in quantitative results. Since the result will be the number or value of the number of the specified problem; the problems chosen for optimization are in the form of a mathematical model. The general purpose of optimization is to find the maximum or minimum value of the objective function and to find the value of the objective function under the constraints. Therefore, the important thing for optimization is to define the objective function and constraints for finding the minimum or maximum values.

2.1.4.1   Design variable

Design variable is a numerical input that is allowed to change during the design optimization to achieve the most appropriate solution. The design variable is defined to describe the characteristics of the system like temperature, concentration, size, and flow rate. Defining the design variables must choose the correct variable in the problem of a system.

2.1.4.2   Objective function

The objective function, a mathematical equation, consists of a design variable used to find the value of the variable at the maximum or minimum point of the objective function. The objective function can be written following:

Static optimization: $y = f(x, u)$ (2.4)

Dynamic optimization: $J = F(x(t), u(t))$ (2.5)

The objective function of static optimization consists of the independent variable (x) and the dependent variable (y) calculated by the relationship of the function (f(x)) as shown in Eq. 2.4. The functional (J) is defined as an objective function of dynamic optimization, which depends on the function x(t) as shown in Eq. 2.5.

2.1.4.3   Constraints

In general, the constraints are divided into two types: external constraints and internal constraints. External constraints are limitations of the system that is apart from the control of designers. In contrast, internal constraints are constrained by system designers. The general form of constraints is as follows:

Static optimization: $x_{min} \leq x \leq x_{max}$

$$u_{min} \leq u \leq u_{max}$$ (2.6)

Dynamic optimization: $\qquad x_{\min} \leq x(t) \leq x_{\max}$

$$u_{\min} \leq u(t) \leq u_{\max} \qquad\qquad (2.7)$$

The constraints will be consistent with the variables in the objective function. When the constraints of the function are changed, the answer given by the objective function will also change. Therefore, the values obtained from the objective function must be consistent with the constraints. The constraints are classified by equation signs as equality constraints (=), and the inequality constraints ($\leq$, $\geq$).

2.1.5 Characterization

2.1.5.1 Scanning Electron Microscopy (SEM)

Scanning Electron Microscope (SEM) is an electron microscope. Visualization is done by measuring the electrons reflected from the surface of the sample being surveyed. The image obtained from this SEM machine is a 3-dimensional image, therefore is used to study morphology and detail of the surface characteristics of the sample. It is commonly used to examine the surface appearance of the sample, check the crystal alignment with the electron diffraction receiving system of the scattering, and check the sample changes from the pull. The Energy Dispersive X-ray Spectrometry (EDS or EDX) is also an X-ray detector in SEM which can analyze various elements contained in the sample (Materials Innovation Center, 2019).

2.1.5.2 X-ray photoelectron spectroscopy (XPS)

XPS technique, also known as Electron Spectroscopy for Chemical Analysis (ESCA), is a technique that uses soft X-ray for stimulation of photoelectrons. It can use to analyze the binding energy of the innermost electrons (core electron) because the energy value is the specific value of the atom in each element and depends on the chemical status of that atom The XPS analysis technique can identify the type and chemical status of the element that means the surface area of the substance to be analyzed (Synchrotron Thailand Central Lab, 2019).

2.2 Literature reviews

2.2.1 Vanadium redox flow battery performance

In recent years, VRFB is used as energy storage for renewable energy because it has many advantages over other types of battery; high flexibility, low cost per kilowatt for long term operation, long live cycle, and high depth of discharge. However, this battery is still necessary to be developed to be achieve high efficiency. The development can be 1) internal battery resistance reduction, 2) increase in energy density by increasing the concentration of vanadium ions, 3) selection and development of materials for half-cell and half-cell baffles, 4) selection and development of materials for making containers, and 5) electrode development, etc. Those are used to assemble batteries to obtain low cost and high-performance. However, the general method for electrode development is the electrode treatment that is the management of the functional group on the electrode surface and it enhances the wettability of an electrode. In January 1992, the graphite felt electrodes treated with sulfuric acid and mixed of sulfuric and nitric acid were performed by Sun and Skyllas-Kazacos (Sun & Skyllas-Kazacos, 1992a). They found that acid concentration in the treatment process inversely with cell resistance. The cell resistance affects VRFB performance in terms of the ohmic overpotential of the actual cell voltage. The decrease of ohmic losses leads to the charge voltage reduction and the discharge voltage increase, resulting in the battery efficiency enhancement. In addition, voltage and coulombic efficiency were improved by treated graphite felt electrodes with thermal treatment (Sun & Skyllas-Kazacos, 1992b). Kim et al. (2011) improved battery efficiency by the electrode treatment technique using the mild oxidation, oxygen plasma, and Gamma-ray irradiation treatment and compared with an untreated electrode. Mild oxidation was operated by heat treatment in a furnace at 300-600 °C for 5 hours under the atmosphere. Oxygen plasma is carried out by an inductively coupled radio frequency plasma fabrication reactor. Gamma-ray is a formality of the electromagnetic radiations of high frequency to produce functional groups on the surface of the matter. As a result, the battery using the electrode treated with mild oxidation at 500 °C provided the highest energy efficiency. Figure 2.7 denotes that the mild oxidation and plasma treatment gives much higher voltage and

energy efficiency than the untreated electrode and gamma-ray electrode which relates to the increasing of C-O and C=O functional groups.
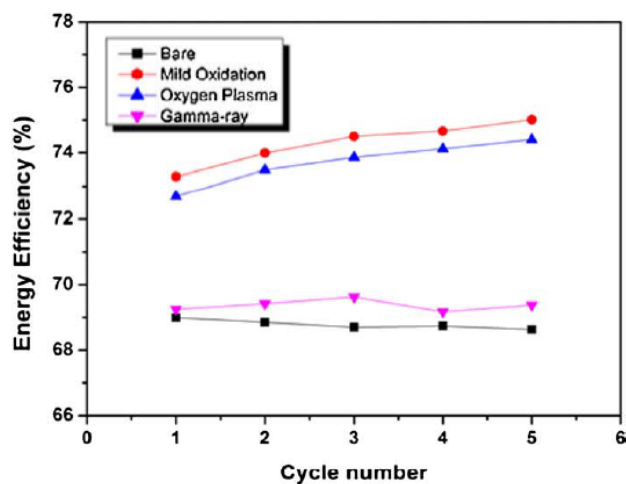
Figure 2.7 The energy efficiency of the battery using untreated electrode, mild oxidation, oxygen plasma, and gamma-ray treatment method (Kim et al., 2011).

Chen et al. (2015) studied the atmospheric pressure plasma jets (APPJs) treatment on graphite felt electrodes that the treated graphite felts significantly improved the energy efficiency and discharge capacity of the VRFB as shown in Figure 2.8. The oxygen functional group in the graphite felt improves the wettability of the graphite resulting in, better electrolyte penetration into the graphite felt electrode and the electrochemical activity improvement on the electrode. This consequently increases the VRFB energy efficiencies. The experimental results demonstrated that APPJ is a rapid, cost-effective, and potentially scalable technique for the surface modification of graphite felts used in VRFBs.
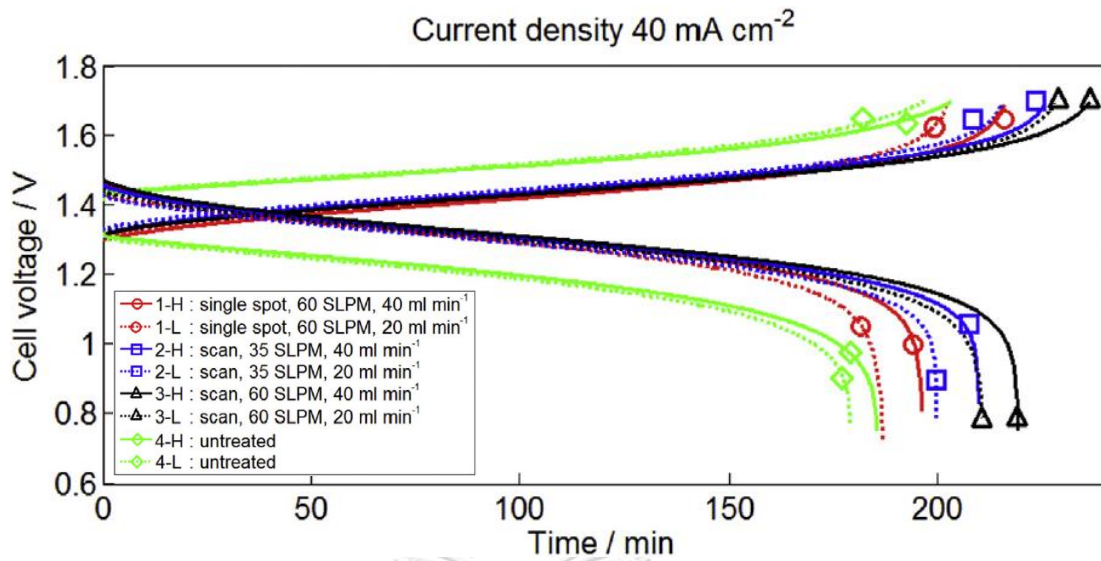
Figure 2.8 Cell voltage improvement of the battery which uses untreated and APPJs treated electrodes (Chen et al., 2015).

Besides, Dixon et al. (2016) studied the comparison of plasma and general method of electrode treatment such as, heat treatment on two types of the electrode; rayon and polyacrylonitrile (PAN). The plasma treatment demonstrated the superior support of the PAN electrode compared to the heat treatment. The plasma treatment improves the electrochemical activity from the increase of the oxygen functional group; however, the heat treatment shows a little oxygen functional group on the surface and the electrode surface area unchanged. Figure 2.9 demonstrates the efficiency and discharge capacity of the electrode treated with plasma were higher than those of the heat treatment method due to the low percentage of capacity loss and high coulombic and energy efficiency. Therefore, the oxygen plasma treatment process could play a major role especially for the activation of PAN-based felts. Although the APPJs was shown as an interesting method for the graphite felt treatment, the optimal temperature for the APPJs process has not been reported in previous research to consider the highest VRFB energy efficiency.
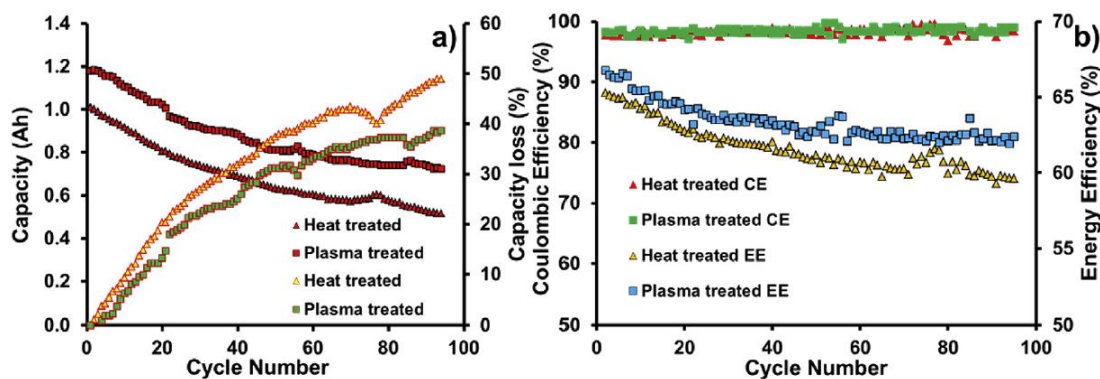
Figure 2.9 The comparison of battery efficiencies between battery using heat and plasma electrode treatments a) discharge capacity and capacity loss b) coulombic and energy efficiency (Dixon et al., 2016).

2.2.1 Operation of vanadium redox flow battery

Unlike conventional batteries, VRFB's energy rating and power rating are independent. The energy rating of the VRFB system depends on the concentration and volume of electrolyte, whereas the number of cell stacks determines the power rating of VRFB. The VRFB system consists of two electrolyte tanks which filled the $V^{2+}/$ V^{3+} and V^{4+}/ V^{5+} in sulfuric acid, a cell stack, and two electric pumps. During the charge/discharge operation, the positive and negative electrolytes are transferred into the cell stack for redox reaction by two electric pumps, in which the energy is stored and released by changing the oxidation state of vanadium ions. The redox reaction will occur at the surface of a porous electrode. The uniform distribution of electrolyte in the porous electrode is important causing the efficient reaction. Several previous studies focused on developing the material such as the electrolyte flow field material to improve battery performance. Xu Zhao and Leung (2013) investigated the three-dimensional model to study the flow field design. The electrolyte with the flow field improved distribution and the overpotential decreased with the increase of the flow rate, which tends to improve battery performance. Kuma and Jayanti (2016) studied the effect of three patterns of the flow field on VRFB performance. The different flow field patterns provide the different directions of the electrolyte through the porous electrode that affects the permeability. Since VRFB is a flow battery, it is undeniable that the electrolyte flow rate can enhance battery efficiency. Ma et al. (2012) showed

the effect of the electrolyte flow rate on battery performance. The electrolyte flow rate increase causes discharge capacity and battery efficiency increase as shown in Figure 2.10. However, the system efficiency of VRFB decreased because the higher electrolyte flow rate consumes the higher pump energy demonstrated in Figure 2.11.
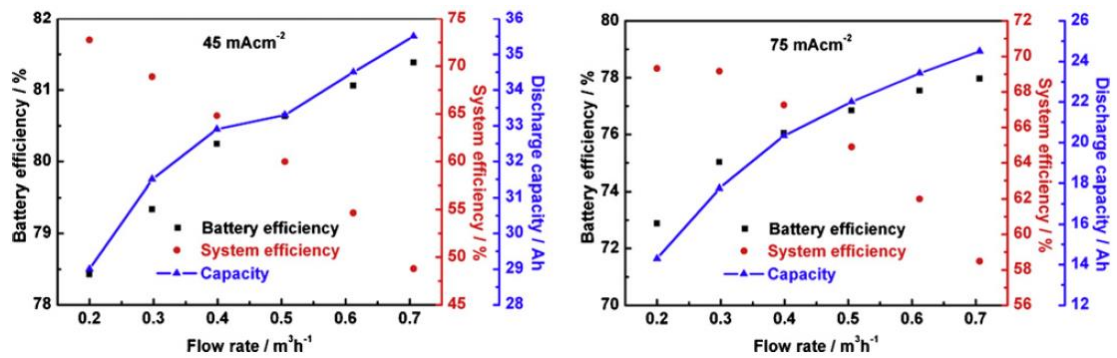
Figure 2.10 Energy efficiency, system efficiency, and discharge capacity at different flow rates (Ma et al., 2012).
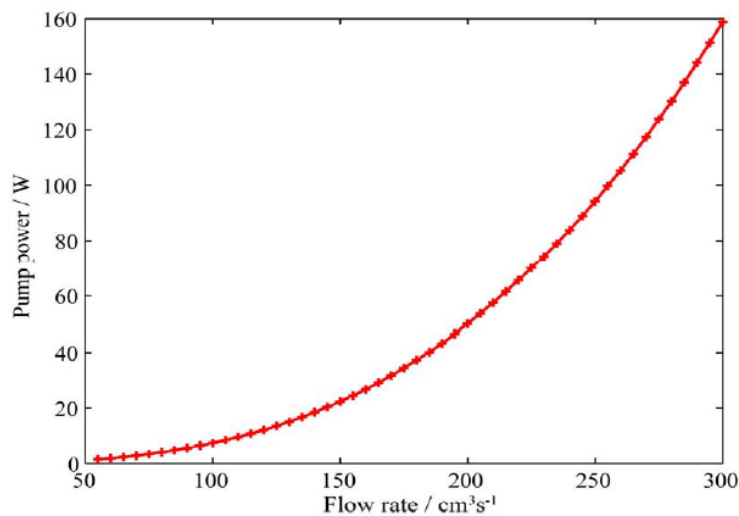
Figure 2.11 Pump power consumptions under various flow rates (Binyu et al., 2013).

The high system efficiency requires considering cell stack power generation and pump power consumption. The pump power consumption is affected via the electrolyte flow rate as shown above. Therefore, flow rate optimization is a reasonable method to improve battery system efficiency. Tang et al. (2014) proposed the mathematical model to study the pressure drop and flow rate optimization in VRFB.

The high electrolyte flow rate influences reduce concentration overpotential at a high state of charge and high state of discharge, but the pump loss is high too. They presented the flow rate optimization that is variable electrolyte flow rate to solve this problem. Figure 2.12-2.13 illustrates the variable flow rate provides higher discharge time due to low concentration loss and requires lower pump energy than the constant flow rate. Since the optimizer must compensate for the dilution of active species concentration and for reducing the concentration overpotential, the electrolyte flow rate will be high at the end of charge and discharge make to high pump power consumption as Figure 2.13. Wang et al. (2018) studied the dynamic control strategy to find the optimal electrolyte flow rate for VRFB system using the optimization algorithm. The minimizing of total power losses was used as the objective function, resulting from the overpotentials, ohmic drops, and power pump consumption, and find the flow factor based on Faraday's law. Hence, they ensured that the control strategy can improve system energy efficiency. Jirabovornwisut et al. (2020) proposed the new electrolyte flow rate control strategy to improve system efficiency that minimizes the power during the charging process and maximizes the power during the discharging process by nonlinear optimization programming. This optimization considers the power of the VRFB stack and pumps power consumption. The proposed optimization can be used to define the optimal flow rate under variations in current density and state of charge.
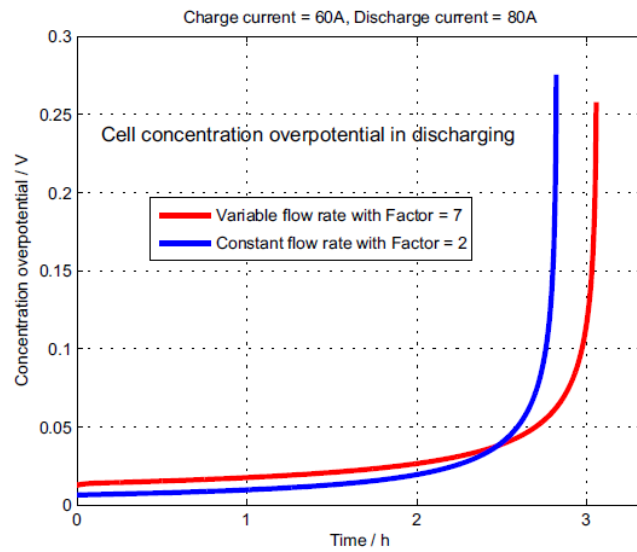
Figure 2.12 Concentration overpotential of variable flow rate compared to a constant flow rate of the discharging process (Tang et al., 2014).
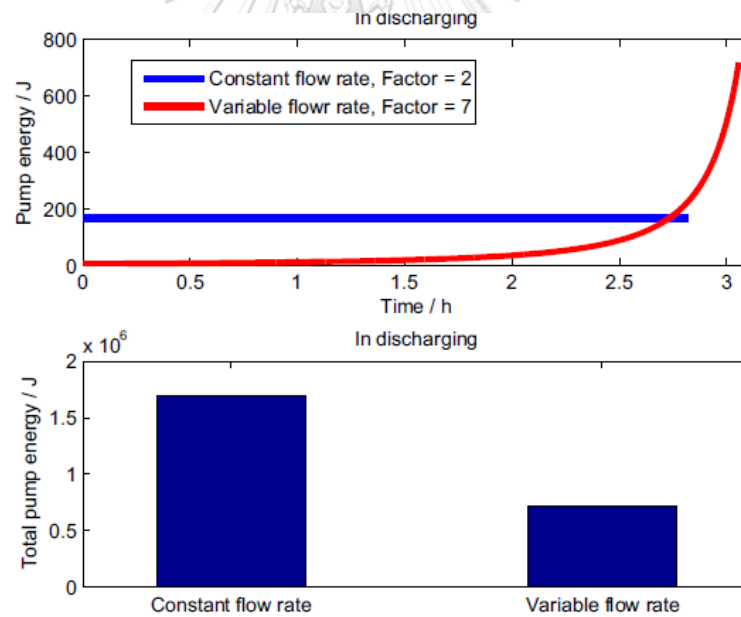
Figure 2.13 Pump power consumption of variable flow rate compared to a constant flow rate of the discharging process (Tang et al., 2014).

2.2.2 Artificial neural network (ANN)

Neural Network (NN) is a network that works like the human brain with ability to be trained, learn, and memorize. Nowadays, several researchers use NN to predict data in many fields, such as weather forecasts, agriculture, economics, geography, and energy. Even though the mathematical model is absent, the NN can effectively solve complex mathematical models' problem, and get accurate and precise answers because it is working as a black box model which can be trained with experimental results. For example, Abolhassani Monfared et al. (2006) performed the equivalent circuit parameter prediction of a lead-acid battery using Neural Network (NN) which the state-of-charge (SOC) is a network input. They confirm that the NN can perfectly predict. Lim and Kang (2018) studied the comparison of the conventional heat transfer model and multilayer ANN analysis of backpropagation to analyze the accelerated control cooling process, and the accuracy improvement of finish cooling temperature prediction by the ANN 3 layers is evaluated. This result show ANN analysis provides an accuracy that improved 2.74 times than the heat transfer model. It was concluded that the heat transfer model could be replaced by the neural network method of 3 layers (one input-layer, one hidden-layer, one output-layer) with the trained weights for the precise control cooling. Mjalli et al. (2007) presented the black box neural network model (ANN) as an actual wastewater plant process model. NN model was trained and validated with plant scale data from a local wastewater treatment plant. The NN model provided accurate results. Furthermore, the NN has several architectures such as the Feedforward model, multilayer RNN, Elman RNN, and NARX ANN. Bonfitto et al. (2019) used the ANN for state-of-charge estimation in lithium-ion batteries which had presented the comparison of the NN architectures. They performed the NARX model takes a little training time, gives a low maximum relative error, and uses small memory as shown in Figure 2.14. Khamis and Abdullah (2014) forecasted wheat price using the NARX model compared to the backpropagation model (BP). As a result, the NARX model provides higher R (close to 1) and lower MSE than BP that is the best prediction model.

In addition, the NN training algorithm is a vital role in training performance. Levenberg-Marquardt (LM) algorithm is regarded as the fastest, the best predictor,

and used small memory, guaranteed from the research of de Ramón-Fernández et al. (2020). They used NN to predict the power of Microbial fuel cell (MFC) and compared training algorithm include Quasi-Newton (QN), Levenberg-Marquardt (LM), and Conjugate Gradient (CG). They varied the hidden nodes from 3 to 12 nodes and ran 100 times of each algorithm to find the best model. They found that the best number of the node of the LM algorithm is 8 nodes, while the QN and CG had 9 and 11 nodes, respectively. Therefore, the LM algorithm used a small training time but offered the highest accuracy observed from the highest correlation coefficient (R) in Figure 2.15. Mohammadi et al. (2019) also found the similar results. They applied NN with Pyrene removal from the soil process. They operated NN training with different training algorithms such as Scaled Conjugate Gradient (SCG), Resilient Backpropagation (RP), Gradient Descent (GD), Conjugate Gradient with Powell-Beale Restarts (CGB), and Levenberg Marquardt (LM). LM algorithm shows the highest correlation coefficient (R) of NN training and testing data as seen in Figure 2.16.
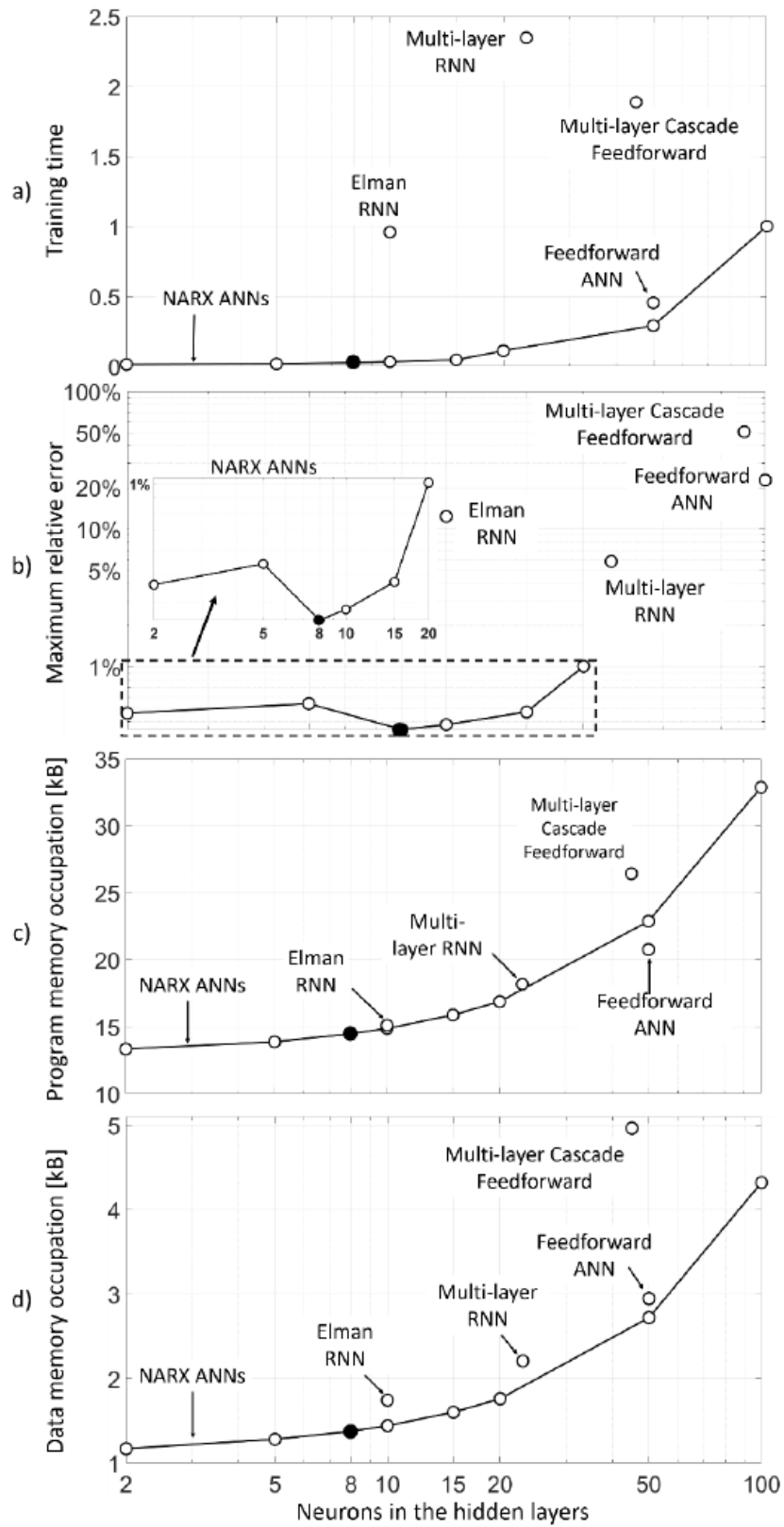
Figure 2.14 The comparison of ANN architectures (Bonfitto et al., 2019).
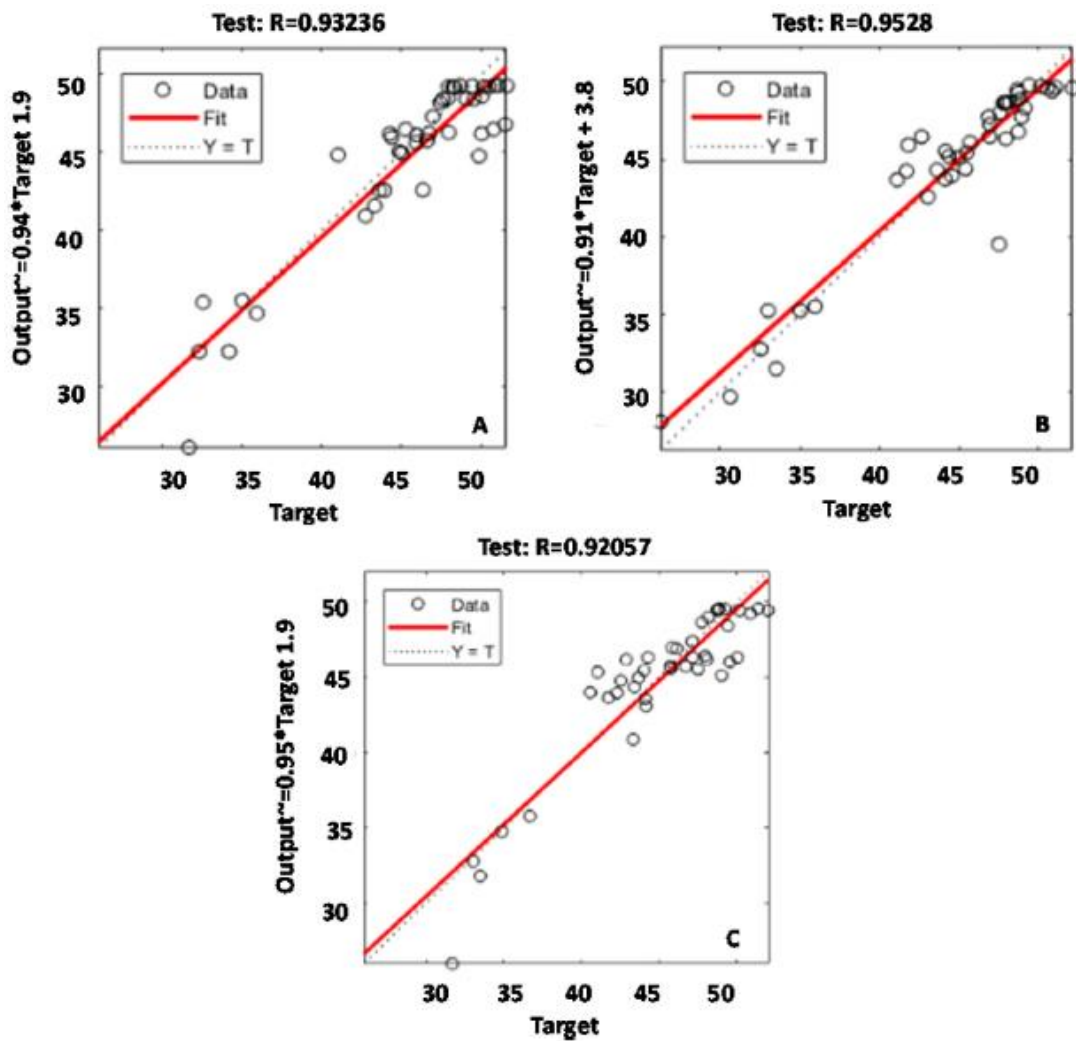
Figure 2.15 The training correlation coefficient (R) of a) QN algorithm b) LM algorithm c) CG algorithm (de Ramón-Fernández et al., 2020).

Training Algorithm	R (all data)	R (test data)
Quasi-Newton (*BFGS*[a])	0.930	0.942
Conjugate Gradient with Powell-Beale Restarts (CGB)	0.797	0.559
Fletcher-Reeves Conjugate Gradient (CGF)	0.944	0.493
Polak-Ribiere Conjugate Gradient (CGP)	0.933	0.901
Levenberg Marquardt (LM)	0.972	0.998
Scaled Conjugate Gradient (SCG)	0.944	0.989
Resilient Backpropagation (RP)	0.968	0.971
Gradient Descent (GD)	0.410	0.473

[a] **BFG**, the Broyden–Fletcher–Goldfarb–Shanno (*BFGS*) algorithm.

Figure 2.16 The comparison of different NN training algorithms (Mohammadi et al., 2019).

CHAPTER 3

EXPERIMENTAL METHOD

The experiment is divided into two parts. First, the measurement of battery cell voltage and calculate the battery efficiency as the coulombic efficiency, voltage efficiency, energy efficiency, and discharge capacity. After the voltage measurement is completed, the electrode is brought out of the cell to analyze the characteristic of the electrode untreated and treated by APPJs at 450°C, 550°C, 650°C, and H_2SO_4 treatment method.

3.1   Battery voltage measurement

3.1.1   Cell component

The single-cell components consist of seven parts, i.e., two end plates, two current collectors, two flexible graphite foils, two graphite plates, two flow field patterns, two electrodes, and a membrane. The current collector of a VRFB is made of copper covered by gold as it can resist the corrosion caused by an acid electrolyte and is inert material to redox reactions. It is placed in the block of the flexible graphite foil. Next, the graphite plate is the plate of the electrolyte flowing in and out of the cell. The active species are uniformly distributed to an electrode via the PVC flow field to decrease the concentration overpotential. In this work, the graphite felt electrode is selected to be used in the VRFB system because of its high stability and surface area. The positive and negative half-cells are separated by a Nafion117 membrane (Dupont, USA). Finally, the VRFB cell is sandwiched by two end plates and locked by the eight nuts.
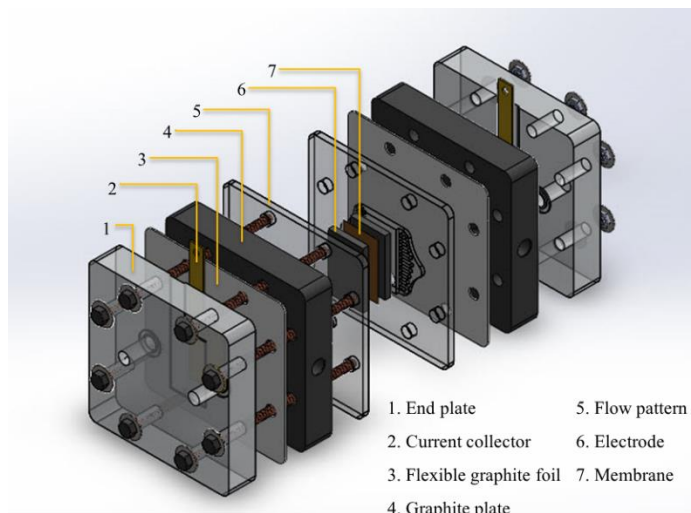
Figure 3.1 Cell assembly of vanadium redox flow battery.

3.1.2 Electrolyte preparation

Electrolyte solution prepared from 37.731 g. of 1.5 M $VOSO_4$ (the $VOSO_4$ powder shows in Figure 3.2.) stirred with deionizing water and 29.78 g. of 2.0 M H_2SO_4 at room temperature. After that, the deionized water is added into the mixture solution until the total volume reached 150 ml, then the initial electrolyte volumes are divided as positive and negative electrolytes with 100 and 50 ml, respectively. Before performing the experiments, nitrogen is introduced to the flask to prevent air oxidation. The pre-charging is an important step to prepare the oxidation state of vanadium ions from V^{4+} to be V^{5+} and V^{2+} in the positive and negative electrolytes, respectively. The current density for the pre-charging process is 80 mA/cm^2 with CC-CV mode. Finally, the volume of the positive and negative electrolytes is separated into 50 ml for each flask.
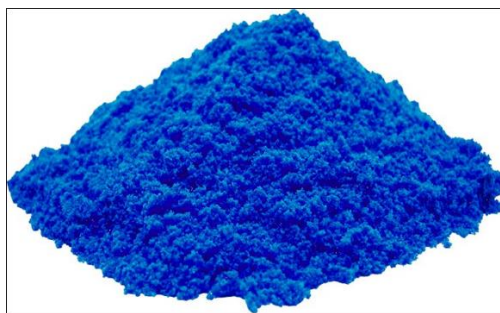
Figure 3.2 Vanadium sulphate (VOSO4) powder.

3.1.3 Electrode and membrane preparation

3.1.3.1 APPJs treatment

The APPJs schematic is shown in Figure 2.2. APPJs treatment is operated with a voltage of 275 V and the on/off duty cycle of 7/33 microsecond. The N_2 flow rate is adjusted for various peak temperatures; 450°C, 550°C, and 650°C. However, electrodes treated with APPJs are performed by outer manufacture.

3.1.3.2 H₂SO₄ treatment

The H_2SO_4 electrode is prepared by soaking the ($25 \times 40 \times 6.5$ mm^3) graphite felt electrode in 2 M of H_2SO_4 at 60°C for 12 hours, and then the electrode is rinsed with deionized water. After that, the electrode is dried by squeezing.

3.1.3.3 Membrane preparation

The Nafion117 membrane is cleaned with 2 M H_2SO_4 at 60°C for 24 hours, then rinse with deionized water.

3.1.4 Cell assembly and pre-charge

After the cell stack is assembled, the cell stack is connected to the AC/DC battery tester (PFX2021, Kikusui Electronic, Japan) by plugging the tester electric wires at the current collector of the positive and negative half cells. Before performing the experiments, nitrogen is introduced to the flask to prevent air oxidation. The pre-charging is an important step to prepare the oxidation state of vanadium ions from V4+ to be V5+ and V2+ in the positive and negative electrolytes, respectively. The

positive and negative electrolytes are pumped from the tanks into the cell stack and flow back into the tank by two diaphragm pumps (SMART Digital DDA 7.5-16AR-PVC/V/C, Grundfos, Denmark). The electrolytes are pumped into the stack to oxidation-reduction reactions, then the electrolyte will recirculated into the original positive and negative electrolyte tank causing to decreasing of electrolyte concentration. The pre-charging process starts after the electrolyte is distributed in the cell by operating the pump without the current. The Constant Current - Constant Volt (CC-CV) mode with a current density of 80 mA/cm^2 is used for the pre-charging process. The CC-CV mode has two steps. First, the battery is charged at a constant current that is CC mode until the battery voltage reaches the upper limit. After that, it switches into CV mode that charges the battery at the constant voltage at the upper limit, and the current decrease until reach cut-off current. Now positive and negative electrolytes are converted into V^{5+} and V^{2+}, respectively. Finally, the volume of the positive and negative electrolytes is separated into 50 ml for each flask.

3.1.5 Battery performance measurement

The VRFB voltage is measured and recorded every 1 second by AC/DC battery tester (PFX2021, Kikusui Electronic, Japan), using the constant current density of 40 mA/cm^2 and the cut-off voltage for the upper and lower limit of 0.7 and 1.7 V, respectively. The VRFB performances are calculated as given in Table 3.1. The coulombic efficiency (CE) as in Eq. 3.1 is the ratio of discharge capacity to charge capacity that represents the efficiency of total usable charge energy. The voltage efficiency (VE) indicates the ratio of the discharge voltage to the charge voltage as shown in Eq. 3.2. The energy efficiency (EE) is a multiple of CE and VE (Eq. 3.3) that represents the ratio of discharging power to charging power. Eq. 3.4 is the discharge capacity calculation.

3.1.6 Graphite felt electrode characterization

Scanning Electron Microscopy (SEM) is used to analyze the surface morphology of the untreated and treated graphite felt electrodes. Moreover, the percentage of oxygen on electrodes is performed by Energy Dispersive X-ray Spectrometry (EDX) technique from SEM analysis. The percentage of C, O, N

elements and the amount of functional group on the electrode surface as C-O, C=O, and -COOH are analyzed by X-ray photoelectron spectroscopy (XPS). The electrode permeability is observed by dropping water on each electrode.

Table 3.1 The equation used to determine the battery performance.

Battery performance	Equation	
Coulombic efficiency (CE)	$\dfrac{\int i_{discharge}(t)dt}{\int i_{charge}(t)dt}$	(3.1)
Voltage efficiency (VE)	$\dfrac{\int V_{discharge}(t)dt}{\int V_{charge}(t)dt}$	(3.2)
Energy efficiency (EE)	CE×VE	(3.3)
Discharge capacity (DC)	$\int i_{discharge}(t)dt$	(3.4)

จุฬาลงกรณ์มหาวิทยาลัย

CHULALONGKORN UNIVERSITY

CHAPTER 4

MODELING OF VANADIUM REDOX FLOW BATTERY

4.1 Mathematical model

4.1.1 Model assumptions

The model assumptions are necessary to simplify developing mathematical modeling. In this study, the simulations will be carried out in MATLAB software.

(1) The electrolyte is perfectly mixed that causes uniform concentration in all positions.

(2) The electrolyte density and viscosity are constant.

(3) The electrolyte volume in each half-cell and tank are constant.

(4) Side reactions caused by diffusion of ions across the membrane are instantaneous.

(5) The electrolyte imbalance due to the gassing side reaction is neglected.

(6) The anodic and cathodic transfer coefficient is equal to 0.5 due to symmetric electron transfer.

(7) Properties of an electrode (electrode thickness, poor diameter, electrode conductivity, and electrode surface area) are constant.

(8) Temperature is assumed to constant at room temperature.

4.1.2 Mole balance

The cell membrane's role is to separate negative and positive half-cell battery. Usually, the cell membrane is designed to allow only the proton can pass through and the vanadium ions are impervious. In fact, it cannot avoid or protect the vanadium ion transfer across the membrane completely. As a result, the battery self-discharge will take place that causes the loss of coulombic efficiency. The capacity loss occurs because of the difference in rates of ions diffusion leading to the accumulation of ions

in one half-cell and dilution in one half-cell. When a reaction occurs, the ions in one side may be depleted first resulting in decreased in battery efficiency.

The diffusion of V^{2+} and V^{3+} from the negative to positive half-cell will result in the following self-discharge reactions (Yan et al., 2016):

$$V^{2+}+2VO_2^+ +2H^+ \rightarrow 3VO^{2+}+H_2O \tag{4.1}$$

$$V^{3+}+VO_2^+ \rightarrow 2VO^{2+} \tag{4.2}$$

$$V^{2+}+VO^{2+}+2H^+ \rightarrow 2V^{3+}+H_2O \tag{4.3}$$

The diffusion of VO^{2+} and VO_2^+ from positive to negative half-cell will result in the following self-discharge reactions (Yan et al., 2016):

$$VO^{2+}+V^{2+}+2H^+ \rightarrow 2V^{3+}+H_2O \tag{4.4}$$

$$VO_2^+ +2V^{2+}+4H^+ \rightarrow 3V^{3+}+2H_2O \tag{4.5}$$

$$VO_2^+ +V^{3+} \rightarrow 2VO^{2+} \tag{4.6}$$

Base on the above assumption, the cell mole balance equations are Eq. 4.7-4.10 and the tank mole balance equations are Eq. 4.11-4.14 When C_i is vanadium ion concentration, V_c is cell volume, Q_c is electrolyte flow rate in the cell, F is Faraday's law constant, k_i is diffusion coefficient, S is membrane surface area, d is membrane thickness, and i is current density.

$$\frac{V_c}{2}\frac{dC_{V^{2+}}^c}{dt} = Q_c\left(C_{V^{2+}}^t - C_{V^{2+}}^c\right)\pm\frac{i}{F} - k_2\frac{C_{V^{2+}}^c}{d}S - 2k_5\frac{C_{VO_2^+}^c}{d}S - k_4\frac{C_{VO^{2+}}^c}{d}S \tag{4.7}$$

$$\frac{V_c}{2}\frac{dC_{V^{3+}}^c}{dt} = Q_c\left(C_{V^{3+}}^t - C_{V^{3+}}^c\right)\pm\frac{i}{F} - k_3\frac{C_{V^{3+}}^c}{d}S + 3k_5\frac{C_{VO_2^+}^c}{d}S + 2k_4\frac{C_{VO^{2+}}^c}{d}S \tag{4.8}$$

$$\frac{V_c}{2}\frac{dC_{VO^{2+}}^c}{dt} = Q_c\left(C_{VO^{2+}}^t - C_{VO^{2+}}^c\right)\pm\frac{i}{F} - k_4\frac{C_{VO^{2+}}^c}{d}S + 3k_2\frac{C_{V^{2+}}^c}{d}S + 2k_3\frac{C_{V^{3+}}^c}{d}S \tag{4.9}$$

$$\frac{V_c}{2}\frac{dC_{VO_2^+}^c}{dt} = Q_c\left(C_{VO_2^+}^t - C_{VO_2^+}^c\right)\pm\frac{i}{F} - k_5\frac{C_{VO_2^+}^c}{d}S - 2k_2\frac{C_{V^{2+}}^c}{d}S - k_3\frac{C_{V^{3+}}^c}{d}S \tag{4.10}$$

$$V_t \frac{dC_{V^{2+}}^t}{dt} = Q_c \sum C_{V^{2+}}^c - Q_s C_{V^{2+}}^t \qquad (4.11)$$

$$V_t \frac{dC_{V^{3+}}^t}{dt} = Q_c \sum C_{V^{3+}}^c - Q_s C_{V^{3+}}^t \qquad (4.12)$$

$$V_t \frac{dC_{VO^{2+}}^t}{dt} = Q_c \sum C_{VO^{2+}}^c - Q_s C_{VO^{2+}}^t \qquad (4.13)$$

$$V_t \frac{dC_{VO_2^+}^t}{dt} = Q_c \sum C_{VO_2^+}^c - Q_s C_{VO_2^+}^t \qquad (4.14)$$

4.1.3 Electrochemical model

The open-circuit voltage is the maximum operating voltage of the cell when it has no current. The open-circuit voltage is a relationship between the electrical potential occurring in the cell and the standard potential (E^0) represented by Nernst Equation (Eq. 4.15) which is a different potential of the positive (E_p) and negative (E_n) electrodes that correlate with active species concentration (C_i) as shown in Eq. 4.16 and Eq. 4.17, respectively.

$$E^{OCV} = E_p - E_n = E^0 + \frac{RT}{nF} \ln\left(\frac{C_{V^{2+}} C_{VO_2^+} C_{H^+}^2}{C_{V^{3+}} C_{VO^{2+}}} \right) \qquad ; E^0 = 1.259\ V \qquad (4.15)$$

$$E_p = E_p^0 - \frac{RT}{nF} \ln\left(\frac{C_{VO^{3+}}}{C_{VO_2^+} C_{H^+}^2} \right) \qquad ; E_p^0 = 1.004\ V \qquad (4.16)$$

$$E_n = E_n^0 - \frac{RT}{nF} \ln\left(\frac{C_{V^{2+}}}{C_{V^{3+}}} \right) \qquad ; E_n^0 = -0.255\ V \qquad (4.17)$$

During the charge-discharge operation, the voltage loss will take place normally. The overpotential describes the discrepancy of equilibrium potential or open-circuit voltage and actual measure potential that is the voltage loss shown in Eq. 4.18. The overpotential has 3 terms; activation overpotential (η_{act}), concentration overpotential (η_{con}), and ohmic loss (η_{ohm}) as shown in Eq. 4.19.

$$\eta = E^{cell} - E^{OCV} \tag{4.18}$$

$$\eta = \eta_{act} + \eta_{con} + \eta_{ohm} \tag{4.19}$$

Activation overpotential describes the kinetics of electrochemical reactions that are always present and most predominant at low currents. It is a regard for the activation energy required to initiate electron transfer which is explained by the Butler-Volmer equation with symmetric electron transfer assumption; the anodic (α_a) and cathodic (α_c) electron transfer coefficient equal to 0.5, as given in Eq. 4.20 and Eq. 4.21.

$$\eta_{act,p} = \frac{2RT}{nF} \sinh^{-1}\left(\frac{i}{2i_{0,p}}\right) \tag{4.20}$$

$$\eta_{act,n} = \frac{2RT}{nF} \sinh^{-1}\left(\frac{i}{2i_{0,n}}\right) \tag{4.21}$$

when the exchange current density of anodic and cathodic is the current in the absence of net electrolysis and at zero overpotential are illustrated in Eq. 4.22 and Eq. 4.23, respectively.

$$i_{0,p} = Fk_p C_{VO^{2+}}^{(1-\alpha_c)} C_{VO_2^+}^{(\alpha_c)} = Fk_p \sqrt{C_{VO^{2+}} C_{VO_2^+}} \tag{4.22}$$

$$i_{0,n} = Fk_n C_{V^{2+}}^{(1-\alpha_a)} C_{V^{3+}}^{(\alpha_a)} = Fk_n \sqrt{C_{V^{2+}} C_{V^{3+}}} \tag{4.23}$$

Mass transfer limitation describes by the concentration overpotential that relies on the concentration gradient between the bulk electrolyte solution and electrolyte solution at the electrode surface. It is particularly dominant at the end of the charge and discharge process because the concentrations of the active species for the redox reactions are low. The concentration loss (η_{con}) related to the electrolyte flow rate (in terms of Reynolds number) and active species concentration (C_{bulk}) in which the loss can be determined by Eq. 4.24 for positive half-cell and Eq. 4.25 for negative half-cell. For the concentration C_{bulk}, it follows Table 4.1. The mass transfer coefficient ($k_{m,i}$) of the active species in the carbon fiber electrode is proposed by Eq.

4.26 which was reported by Khazaeli et al. (2015). It depends on the effective diffusion coefficient of reactant (D_i^{eff}) that can be determined by Eq. 4.27, a pore diameter of the electrode (d_f), and Reynolds number (Re).

$$\eta_{con,p} = \frac{RT}{nF} \ln\left(1 - \frac{i}{k_{m,i}nFC_{bulk,p}}\right) \tag{4.24}$$

$$\eta_{con,n} = \frac{RT}{nF} \ln\left(1 - \frac{i}{k_{m,i}nFC_{bulk,n}}\right) \tag{4.25}$$

$$k_{m,i} = \frac{D_i^{eff}}{d_f} 7\,\text{Re}^{0.4} \tag{4.26}$$

$$D_i^{eff} = \varepsilon^{3/2} D_i \tag{4.27}$$

Table 4.1 The using of C_{bulk} in the concentration loss equation.

	Charging process	**Discharging process**
$C_{bulk,p}$	$C_{VO^{2+}}$	$C_{VO_2^+}$
$C_{bulk,n}$	$C_{V^{3+}}$	$C_{V^{2+}}$

The ohmic loss (η_{ohm}) occurs from the electrical current flowing through the resistances of the cell. The ohmic loss is a function of the resistances of each cell component. In the flow battery, it is the summation of electrode resistance, membrane resistance, and electrolyte resistance as shown in Eq. 4.28. The electrolyte conductivity (σ_{elec}) is the function of concentration which can be performed by Eq. 4.29.

$$\eta_{ohm} = i\left(\frac{d_e}{\sigma_e} + \frac{d_{mem}}{\sigma_{mem}} + \frac{d_{elec}}{\sigma_{elec}}\right) \tag{4.28}$$

$$\sigma_{elec} = \frac{F^2}{RT} \sum_i z_i^2 D_i^{eff} C_i \tag{4.29}$$

Therefore, the cell voltage of the VRFB for the charging process is expressed the incorporating the Nernst equation and the overpotential for compensating the voltage loss as shown in Eq. 4.30. In contrast, the overpotential is subtracted from the open-circuit voltage of the cell voltage of the VRFB for the discharging process which is the actual cell voltage that can be used from the battery as shown in Eq. 4.31.

$$E_{cell} = E^0 + \frac{RT}{nF} \ln\left(\frac{C_{V^{2+}} C_{VO_2^+} C_{H^+}^2}{C_{V^{3+}} C_{VO^{2+}}} \right) + \left(\eta_{act} + \eta_{con} + \eta_{ohm} \right) \qquad ; \text{for charge} \tag{4.30}$$

$$E_{cell} = E^0 + \frac{RT}{nF} \ln\left(\frac{C_{V^{2+}} C_{VO_2^+} C_{H^+}^2}{C_{V^{3+}} C_{VO^{2+}}} \right) - \left(\eta_{act} + \eta_{con} + \eta_{ohm} \right) \qquad ; \text{for discharge} \tag{4.31}$$

4.1.4 Pump power model

The total pressure loss for the VRFB positive and negative sides are the summation of pressure loss of all components of the VRFB system as shown in Eq. 4.32 reported by Wang et al. (2018). Where μ is the electrolyte viscosity, h_e is the height of the electrode, ε is the electrode porosity, λ is the permeability of porous electrode, Q is the electrolyte flowrate, and λ_{CK} is the Carman-Kozeny constant as Eq. 4.33.

$$P_{pump} = \Delta p_{pipe} Q + \frac{\mu h_e}{\lambda A_e} Q^2 \tag{4.32}$$

$$\lambda = \frac{d_{ed}^2 \varepsilon^3}{\lambda_{CK} \left(1 - \varepsilon\right)^2} \tag{4.33}$$

For the piping system, the pressure loss in the piping system can be divided into the major loss due to friction and the minor loss associated with the bends, valves, and fittings as expressed by Tang et al. (2014). Normally, the equation in fluid dynamics of pressure loss due to friction in pipes is expressed by the Darcy-Weisbach equation as shown in Eq. 4.34.

$$\Delta p_{pipe}^{major} = f_D \cdot \frac{L}{d} \cdot \frac{\rho v^2}{2} \tag{4.34}$$

where f_D is the Darcy friction factor, L is the length of the pipe, d is the diameter of the pipe, ρ is the density of the fluid and v is the velocity of the flow. For the laminar flow in pipe, the Darcy friction factor can be expressed as Eq. 4.35.

$$f_D = \frac{64}{\text{Re}} \tag{4.35}$$

In addition, the minor loss equation is illustrated in Eq. 4.36 where f is the minor loss coefficient. Therefore, the total pressure losses in pipes are given by Eq. 4.37.

$$\Delta p_{pipe}^{minor} = f \cdot \frac{\rho v^2}{2} \tag{4.36}$$

$$\Delta p_{pipe} = \Delta p_{pipe}^{major} + \Delta p_{pipe}^{minor} \tag{4.37}$$

4.1.5 The battery performance

The battery performance including coulombic efficiency (CE), voltage efficiency (VE), energy efficiency (EE), system efficiency (SE), and discharge capacity (DC) can be defined from Eqs. 4.38-4.42, respectively. Table 4.2 is the parameters for VRFB mathematical model simulations.

$$CE = \frac{\int \left(I_{discharge}(t) \right) dt}{\int \left(I_{charge}(t) \right) dt} \tag{4.38}$$

$$VE = \frac{\int \left(V_{discharge}(t) \right) dt}{\int \left(V_{charge}(t) \right) dt} \tag{4.39}$$

$$EE = CE \times VE \tag{4.40}$$

$$SE = \frac{\int \left(V_{discharge}(t) I_{discharge}(t) - P_{pump}(t) \right) dt}{\int \left(V_{charge}(t) I_{charge}(t) + P_{pump}(t) \right) dt} \tag{4.41}$$

$$DC = \int \left(I_{discharge}(t) \right) dt \tag{4.42}$$

Table 4.2 The parameters for VRFB mathematical model simulations.

Parameter	Symbol	Value	Reference
Electrode			
- Height	h_e	0.04 m	
- Width	w_e	0.025 m	
- Thickness	d_e	0.0065 m	
- Porosity	ε	0.94	
- Pore diameter	d_f	1.0x10⁻⁵ m	
- Conductivity	σ_e	363 S m⁻¹	
Membrane			
- Thickness	d_{mem}	183x10⁻⁶ m	
Electrolyte			
- Tank volume	V_t	0.05 L	
- Density	ρ	1300 kg m⁻³	Khazaeli et al. (2015).
- Viscosity	μ	0.005 Pa s	Khazaeli et al. (2015).
- Diffusion coefficient of V²⁺/V³⁺	$D_{V^{2+}} / D_{V^{3+}}$	2.4 x 10⁻¹⁰ m² s⁻¹	(Khazaeli et al., 2015)
- Diffusion coefficient of VO²⁺/VO₂⁺	$D_{VO^{2+}} / D_{VO_2^+}$	3.9x 10⁻¹⁰ m² s⁻¹	(Khazaeli et al., 2015)
Electrochemistry			
- Standard potential for the V²⁺/V³⁺ reaction	E_n^0	-0.255 V	
- Standard potential for the VO²⁺/VO₂⁺ reaction	E_p^0	1.004 V	

- Standard rate constant for the negative electrode	$k_{0,n}$	2.6×10^{-6} m s^{-1}	(Chen et al., 2014)
- Standard rate constant for the positive electrode	$k_{0,p}$	6.8×10^{-7} m s^{-1}	(Chen et al., 2014)
- Reference temperature	T_{ref}	298.15 K	
- Stack temperature	T_{stack}	298.15 K	
Other			
- Gas constant	R	8.314 J mol^{-1} K^{-1}	
- Faraday's constant	F	96,485 A s mol^{-1}	

4.2 Artificial neural network modeling

The development of an artificial neural network (ANN) based dynamic model of the VRFB system is described in this part. The developed neural network is used to predict the cell voltage of VRFB from the electrolyte flow rate and the sampling time. Figure. 4.1 shows the VRFB model developed in this study. For modeling the nonlinear dynamic system, the nonlinear autoregressive network with exogenous inputs (NARX) is used. NARX model usually uses in the nonlinear dynamic problem that relates to time-series modeling that shows in Eq. 4.43. The standard architecture of NARX is the feeding back of the output to the input feedforward network. However, if the true output is available during the network training, it is used instead of feeding back the estimated output in the series-parallel architecture. The two advantages of this proposed architecture are the input to the feedforward network is more accurate and the resulting network has a pure feedforward architecture, and static backpropagation can be used for training. Figure. 4.2 shows the series-parallel architecture of the VRFB.
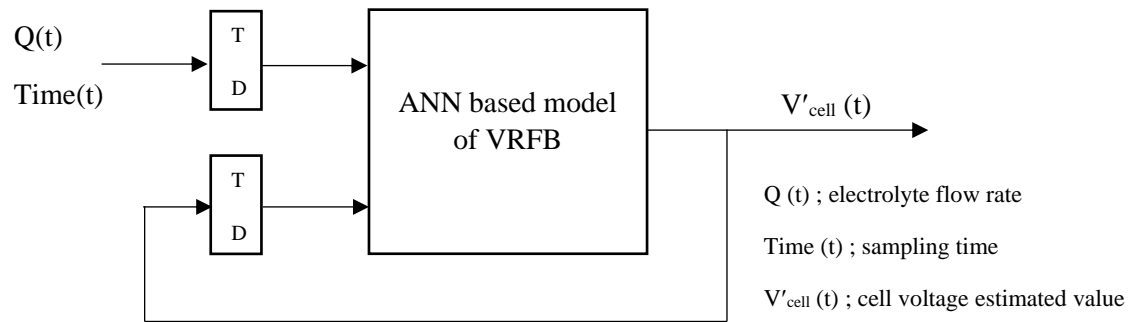
Figure 4.1 The parallel architecture of artificial neural network (ANN) based model of vanadium redox flow battery (VRFB).
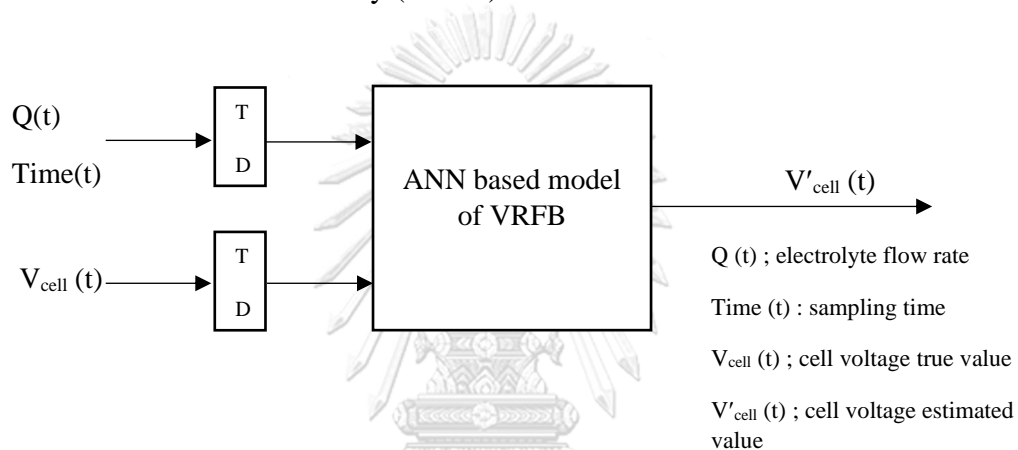
Figure 4.2 The series-parallel architecture of artificial neural network (ANN) based model of vanadium redox flow battery (VRFB).

4.2.1 Collect and prepare the data

Before beginning the neural network design process, sample data are collected and prepared. The correlation between the input and output variables was performed as Figure. 4.3. It shows this input and output variables were a pattern which can be used to train the neural network. Since the neural network cannot be efficient in the non-pattern input and output variable, the correlation proving is necessary for using the variable from the experimental data that unknown its correlation. Moreover, selecting the training data covering the range of predicting is very important because the network does not have the ability to accurately extrapolate when it out of the training data range. Therefore, we need to make the input and target values covering the range that we want to predict. In this work, the random flow rate profiles in the

range of 1-6 L/h are prepared for use to input data. However, the cell voltage in the range of 1.1-1.7 V is used to output or target data. Figure. 4.4-4.6 is an example of the prepared flow rate profile and cell voltage profile for the neural network training. After the data collection, there are two steps of the preprocess before the data are used to train the network for better training efficiency. First, two input data are pairing and arranged into one matrix data. Then, the data is sequenced and divided into 3 subsets for training, validating, and testing into 70%, 15%, and 15%, respectively to avoid the overfitting problem. When the training process is completed, the postprocessing will be applied to convert the data to the appropriate value. The preprocessing and postprocessing flowchart is illustrated in Figure. 4.7.

$$y(t) = f\left(y(t-1), y(t-2),..., y(t-n_y), u(t-1), u(t-2),..., u(t-n_u)\right) \quad (4.43)$$
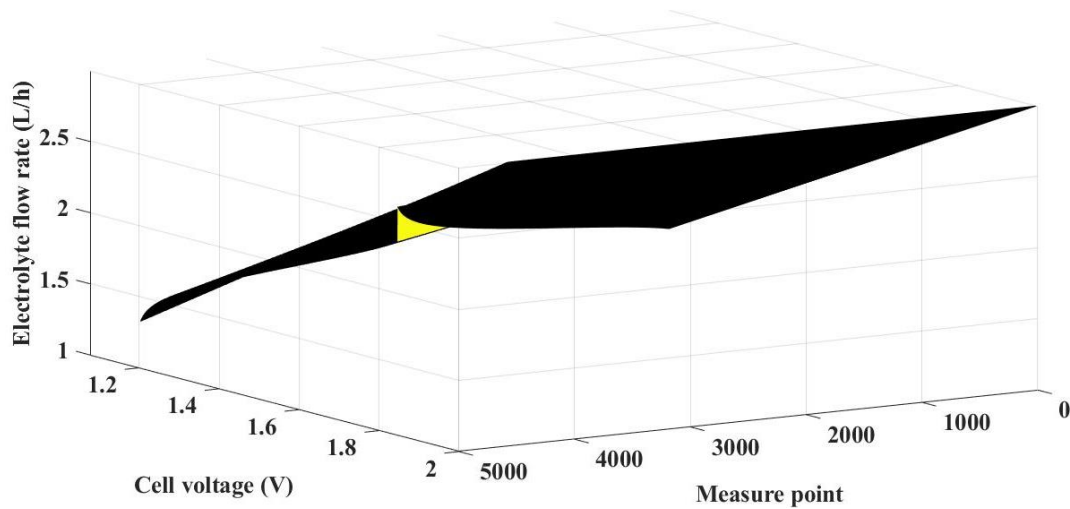
Figure 4.3 The 3D plot of the correlation between input data and output data.
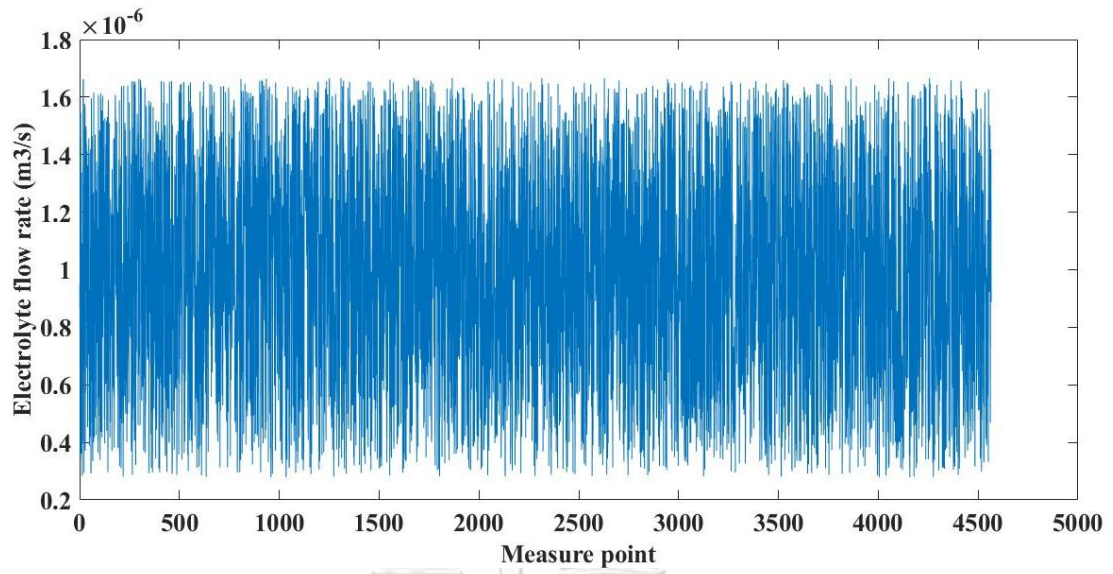
Figure 4.4 The electrolyte flow rate profile for the NN training input.
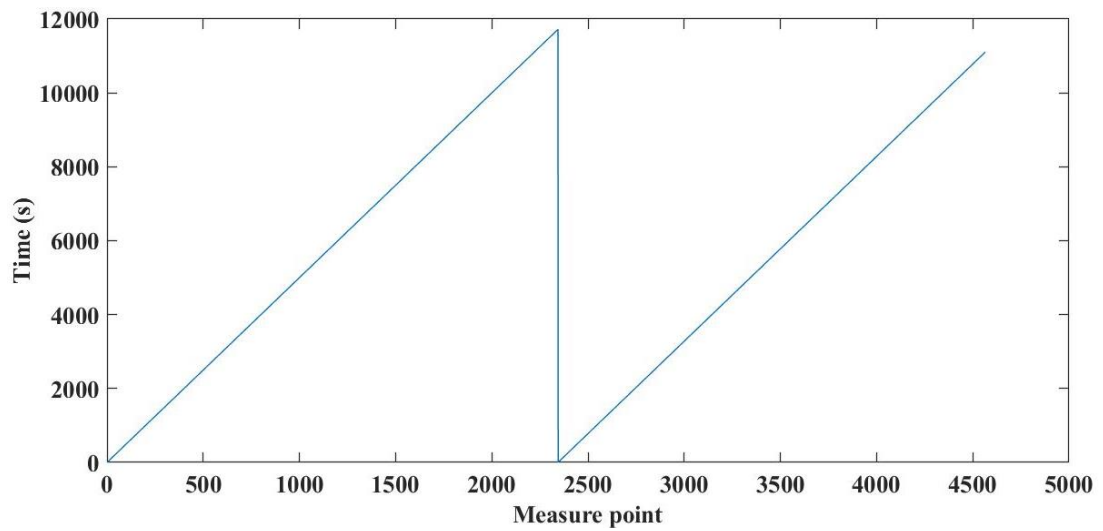
Figure 4.5 The sampling time for the NN training input.
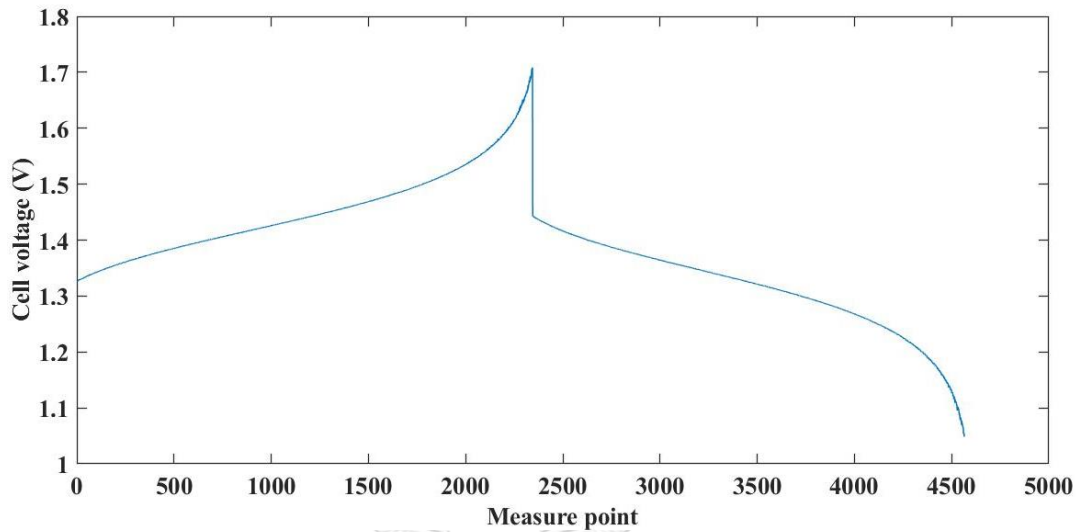
Figure 4.6 The cell voltage profile for the NN training target.
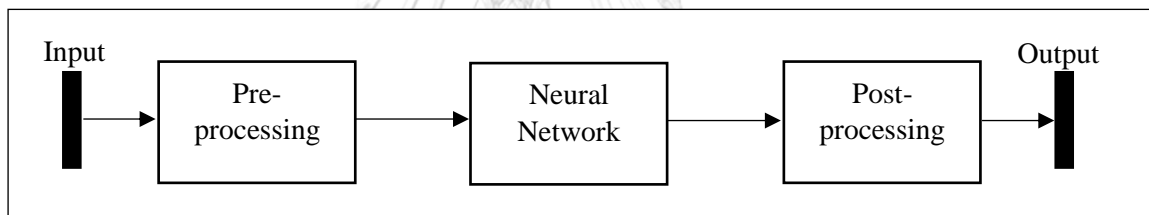
Figure 4.7 The preprocessing and postprocessing flowchart.

4.2.2 Network training

The training of the neural network is tuning the value of the weight and bias of the network to optimize the network performance by using mean square error (mse), the average square error between the network outputs (a) and the target outputs (t) are defined in Eq. 4.44.

$$F = mse = \frac{1}{N}\sum_{i=1}^{N}\left(e_i\right)^2 = \frac{1}{N}\sum_{i=1}^{N}\left(t_i - a_i\right)^2 \tag{4.44}$$

The termination of the training process is considered by the magnitude of the gradient and the number of validation checks. If the goal of the magnitude of the gradient is 1e-5, it means when the gradient is less than 1e-5 the training process will

stop. The number of validation checks indicates the number of successive iterations the failing of validation performance. It means when the validation checks reach 6, the training process will stop. In addition to these two issues, the training will stop when the number of calculation cycles (epoch) reach the set value. The flowchart of Neural Network training illustrates in Figure 4.8.

In this study, the NARX model with time delay 2 steps was used to training the neural network. The Levenberg-Marquardt (trainlm) was applied to the training algorithm and the mean squared error (MSE) was calculated the model performance. The charging process and discharging process were separated training.

4.2.3   Network prediction

After training the neural network model, the testing process will be conducted to prove the NN model accuracy before using this NN model to predict the real data or the required data. When the testing process goes well, this NN model will be recognized as an effective model with accurate predictions and then this NN model can be used for predictions. Before the prediction, it is necessary to prepare the input data form to the same training data form which is the pairing and sequencing of the data. Both one-step ahead and multi-step ahead prediction can be predicted by this NN model.
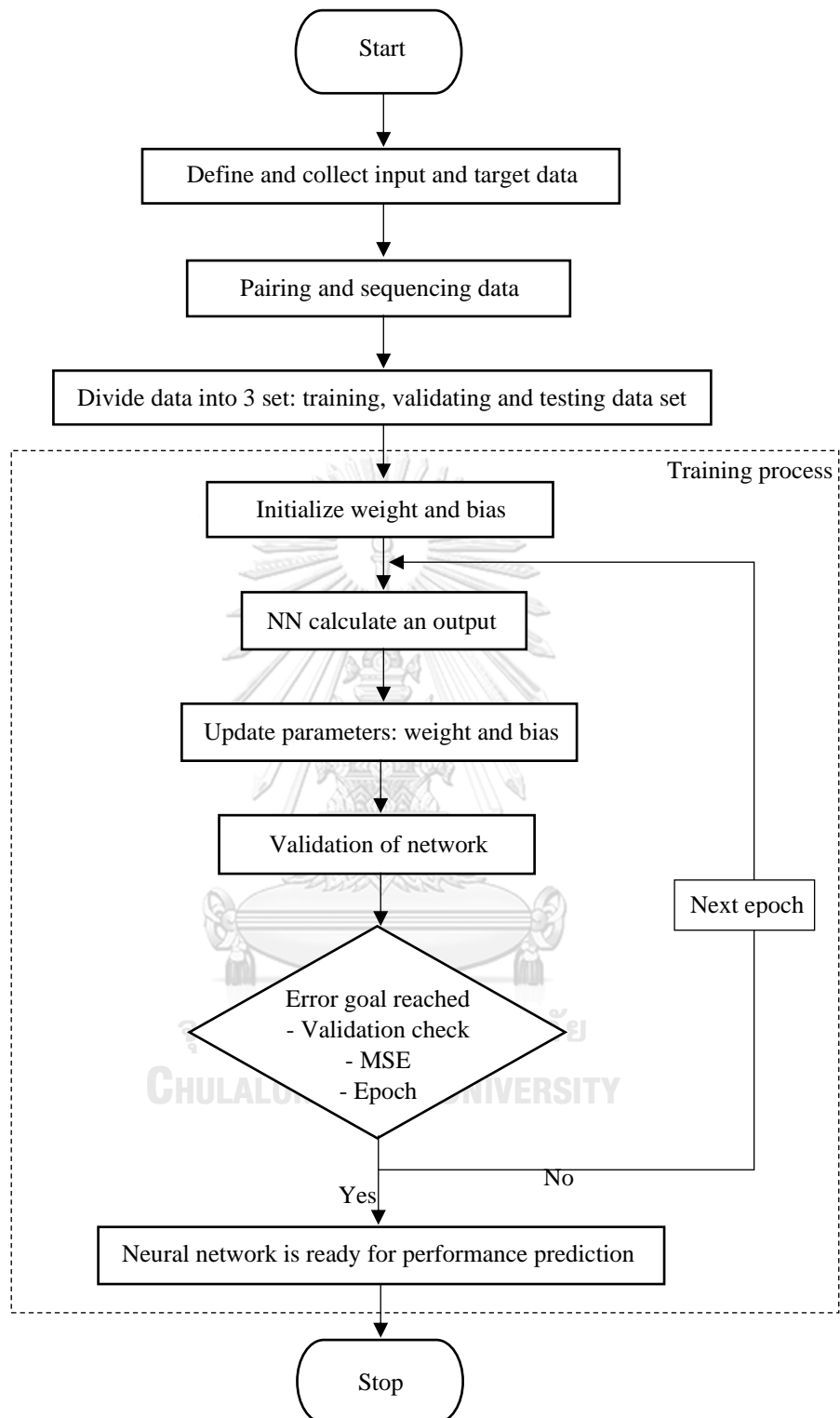
Figure 4.8 The flowchart of Neural Network training.

4.3 Optimization

The sequential discretization approach was applied to solve the offline optimization problem. This optimization was sequenced by dividing time between the initial time to the final time by the number of stages. The SOC 0.05 of vanadium concentration of 1.5 mol/L was operated as the initial vanadium concentration of the first stage and the last concentration of each stage (i) was used as an initial concentration in the next stage (i+1) that integrated into Eqs. 4.7-4.14. However, defining the electrolyte flow rate was necessary to calculate the vanadium concentration using the initial guess of the electrolyte flow rates. After that, the new set of the electrolyte flow rate was determined by the non-linear programming optimization base on the objective function. The minimum applied power (Eq. 4.45) and maximum discharge power (Eq. 4.46) was preferred in this objective function to perform the highest system efficiency (SE, Eq.4.41). Then, the objective function will be compared with the objective function in the previous step, and the optimization process will be stopped when the tolerance reaches the desired value. Therefore, the optimal electrolyte flow rate profile was obtained.

$$\min_{Q(t)} J = \int_{t_0}^{t_f} (IV_{charge} + P_{pump})dt \tag{4.45}$$

$$\max_{Q(t)} J = \int_{t_0}^{t_f} (IV_{discharge} - P_{pump})dt \tag{4.46}$$

For the optimization-based Neural Network model, the trained NN model was used to estimate the cell voltage instead of a mathematical model. After the optimization sequencing was complete, the initial guess of the electrolyte flow rate and time stage were paired and sequenced to use as the input of the NN model. Then, the trained NN model was applied to estimate the battery cell voltage. The voltage estimation of the next stage (i+1) was independent of the previous stage (i) that was different from using a concentration in the recent stage for initial in the next stage of the optimization-based mathematical model. The objective cost that was the minimum power applied (Eq. 4.45) and maximum discharged power (Eq. 4.46) was calculated and compared with the previous stage until reach the desired value. The new set of

electrolyte flow rate was returned to the optimizer. Finally, the optimal electrolyte flow rate for maximum system efficiency was received. The constraints of the optimization based on the mathematical model and the NN model illustrated in Table 4.3.

Table 4.3 The constraints of the optimization based on the mathematical model and the NN model.

Optimization	Charging process	Discharging process
Based on mathematical model	$\dot{x} = f\left(x(t), Q, t\right)$ $x(t_0) = x(0)$ $Q_L \leq Q \leq Q_U$ $V(t_f) = 1.7\,V.$	$\dot{x} = f\left(x(t), Q, t\right)$ $x(t_0) = x(0)$ $Q_L \leq Q \leq Q_U$ $V(t_f) = 1.1\,V.$
Based on NN model	$Q_L \leq Q \leq Q_U$ $V(t_f) = 1.7\,V.$	$Q_L \leq Q \leq Q_U$ $V(t_f) = 1.1\,V.$
Lower (Q_L) – Upper (Q_U) electrolyte flow rate limit	1-6 L/h	

จุฬาลงกรณ์มหาวิทยาลัย

CHULALONGKORN UNIVERSITY

CHAPTER 5

RESULTS AND DISCUSSIONS

In this chapter, we divide into two parts that are the experimental part and the simulation part. In the experimental part, the effect of electrode treatment on vanadium redox flow battery performance is presented and the APPJs treatment and conventional treatment (acid treatment) are compared. In addition, the graphite characterization is analyzed by the Scanning Electron Microscopy (SEM), the Energy Dispersive X-ray Spectrometry (EDX), and the X-ray photoelectron spectroscopy (XPS). In the simulation part, the optimal flow rate of vanadium redox flow battery based on a neural network model is performed by MATLAB programming to take place the highest system efficiency as an objective function. The comparison of the optimization based on NN and mathematical model was conducted.

5.1 Experimental result

5.1.1 The effect of electrode treatment with different APPJ temperature on battery performance.

A single-cell vanadium redox flow battery (VRFB) which an electrolyte volume 50 ml, a volumetric flow rate of electrolyte 3 L/h, and a current density 40 mA/cm^2 was specified on the experimental setting. Figure 5.1 shows the comparison of the VRFB performance which using different electrode treatment. Atmospheric pressure plasma jets (APPJs) electrode treatment demonstrates a higher performance than sulfuric acid (H$_2$SO$_4$) treatment. However, the differential of the temperature of APPJs treatment that 450°C, 550°C and 650°C affects the performance of VRFB. From Figure 5.1a, the discharge capacity of VRFB is decreasing with the number of cycles may be caused by the self-discharge of a battery and with the increasing of APPJs temperature. Consistent with Figure 5.2 that illustrates the discharge voltage of VRFB with difference APPJs temperature, the trends of 550°C and 650°C are suddenly dropped at the end of the discharge while the trend of 450°C is gradually

decreased that may be caused by the effect of the concentration overpotential. Furthermore, since we use constant charge-discharge current density, determining of coulombic efficiency follow Eq. 3.1 is depending on the time of discharge. The ratio of discharging time and charging time in each cycle is closely, the coulombic efficiency does not significantly change when applying with different APPJs temperatures as shown in Figure 5.1b. As a result, an APPJs temperature at 550°C provides the highest energy efficiency (EE). This result will explain in the electrode characterization part.
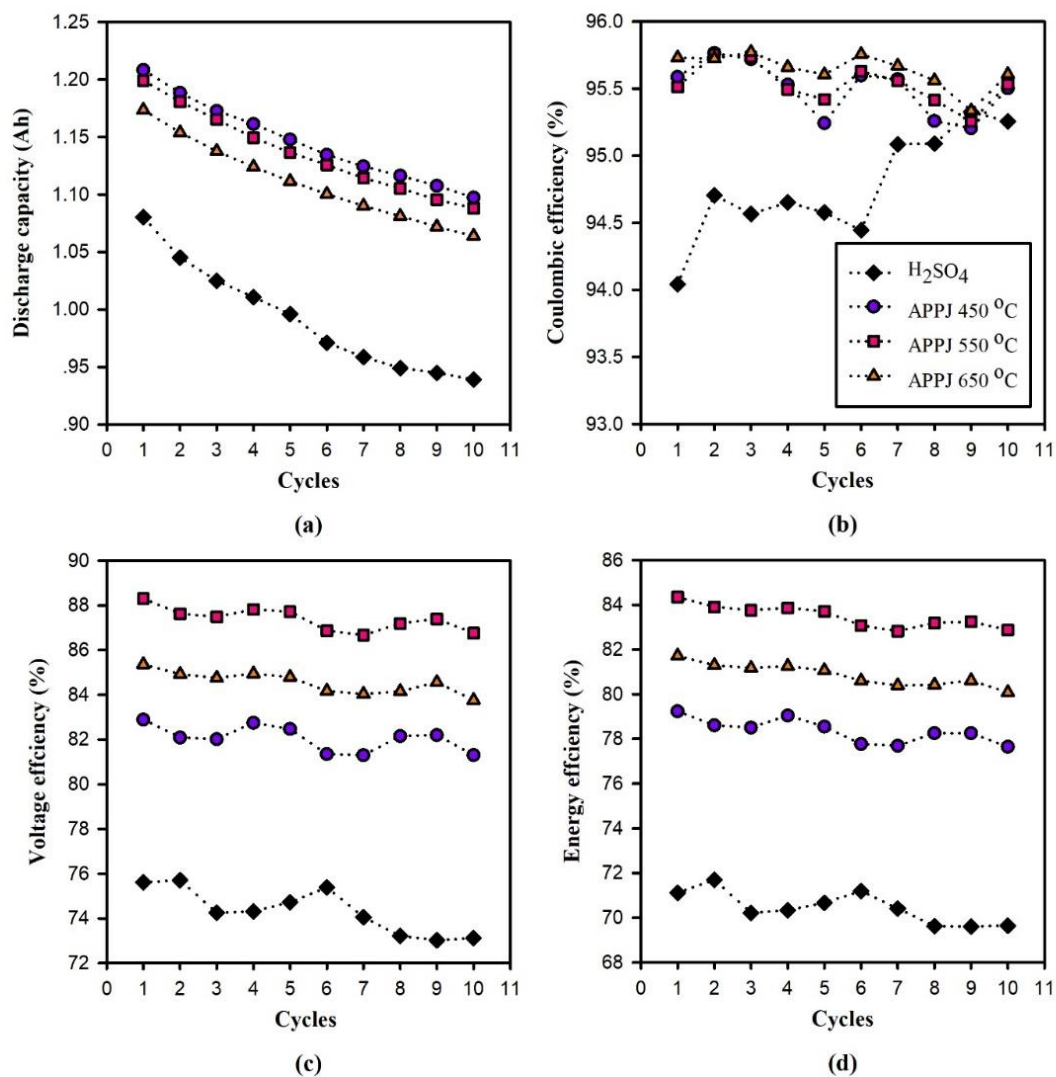
Figure 5.1 The performance of a vanadium redox flow battery with different electrode treatment; (a) Discharge capacity (b) Coulombic efficiency (c) Voltage efficiency and (d) Energy efficiency.
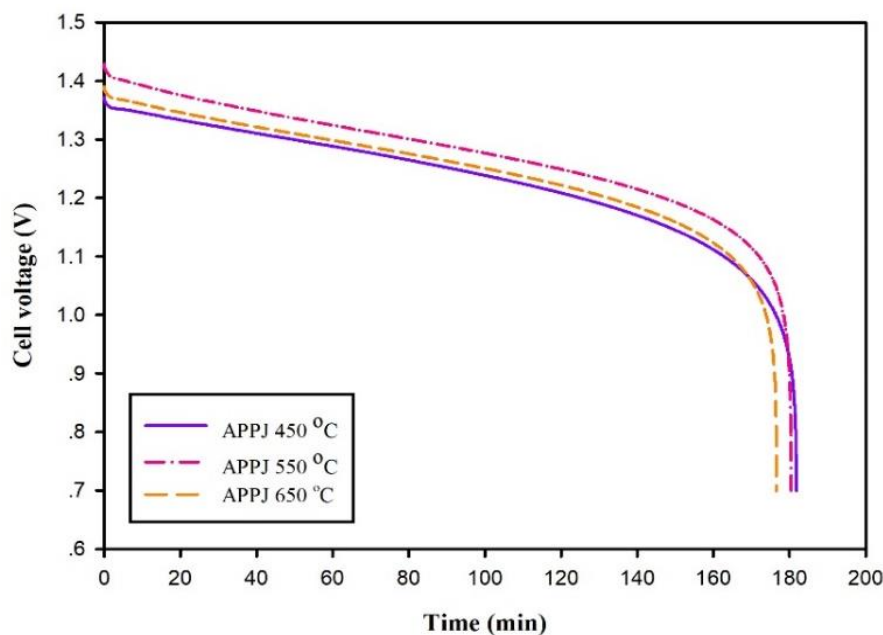
Figure 5.2 The discharge voltage curve of a vanadium redox flow battery with different APPJs temperatures.

5.1.2 Characterization of electrode

From the effect of electrode treatment on VRFB performance in part 5.1.1, we can see that the VRFB performance is enhanced when the electrode treated. However, the performance is increased when using APPJs treatment instead of H_2SO_4 treatment. In this section, we will explain the cause of enhancing VRFB performance.

5.1.2.1 Electrode morphology

The morphology of graphite felt electrode was conducted by a Scanning Electron Microscope (SEM). The surface area and the size of the electrode fiber which un-treated, treated with H_2SO_4, and treated with APPJs at different temperatures are shown in Figure 5.3 and Figure 5.4. From Figure 5.3, the surface area of electrode fibers is still smooth and no visible change after treated under unused and used. Moreover, the size of the electrode fibers is closely that considered no-change as shown in Figure 5.4. As a result, we can conclude that the electrode treatments are not damaging to graphite felt electrode fiber. Figure 5.5 shows the hydrophilicity of 6 electrodes which illustrates the electrode treatment can improve

the wettability. Although both of H_2SO_4 and APPJs treatment can improve wettability, APPJs treatment can better improve than H_2SO_4 which can be observed from the water permeate into the electrode or the contact angle between the water droplet and the electrode surface as in the research of (Zhang et al., 2013). For the effect of different APPJs temperature on wettability, it should be analyzed by contact angle tester to measure the time of permeation. Since a good wettability can reduce the concentration overpotential because the electrolyte will transfer into the electrode more easily, the efficiency of the battery is improved. Therefore, the VRFB which use APPJs treatment is higher performance than H_2SO_4 treatment. However, the improved hydrophilicity is presumably due to the increase of oxygen functional groups on the electrode surface (Kil et al., 2017).

จุฬาลงกรณ์มหาวิทยาลัย

CHULALONGKORN UNIVERSITY
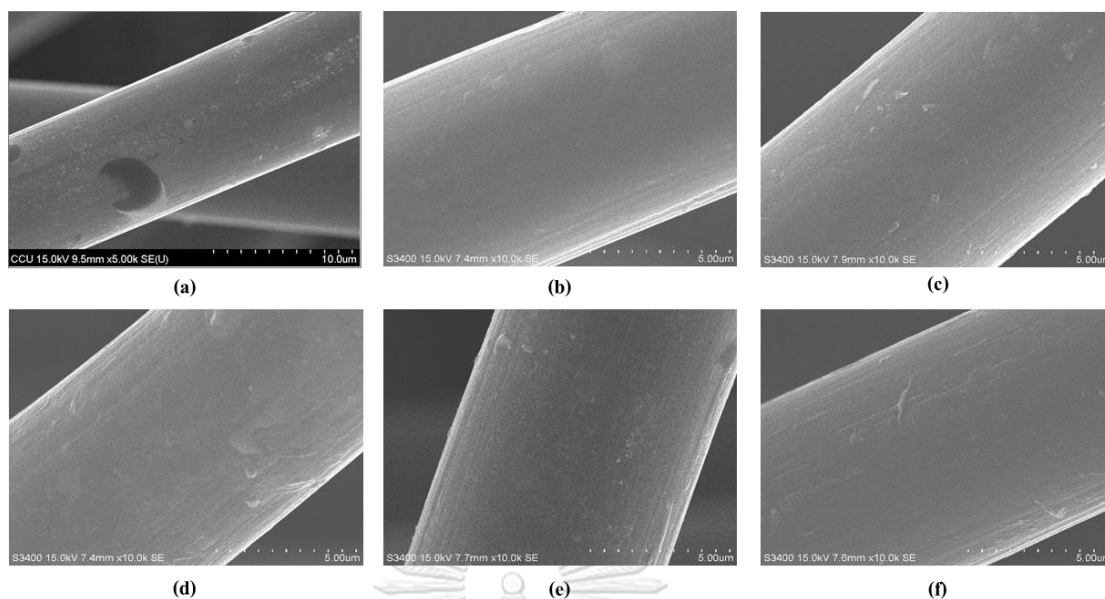
Figure 5.3 SEM images indicate the surface morphology of graphite felt electrodes; (a) un-treated (b) H_2SO_4 treated (c) APPJs 450°C (d) APPJs 550°C (e) APPJs 650°C and (f) APPJs 550°C (used).
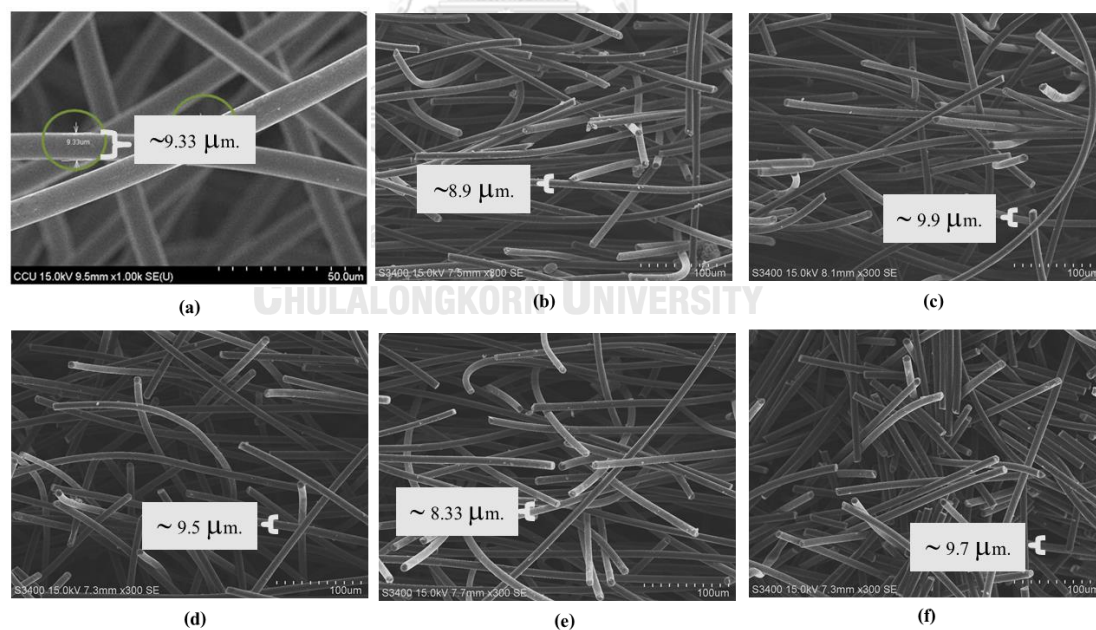
Figure 5.4 SEM images indicate the size of graphite felt electrodes fiber; (a) un-treated (b) H_2SO_4 treated (c) APPJs 450°C (d) APPJs 550°C (e) APPJs 650°C and (f) APPJs 550°C (used).
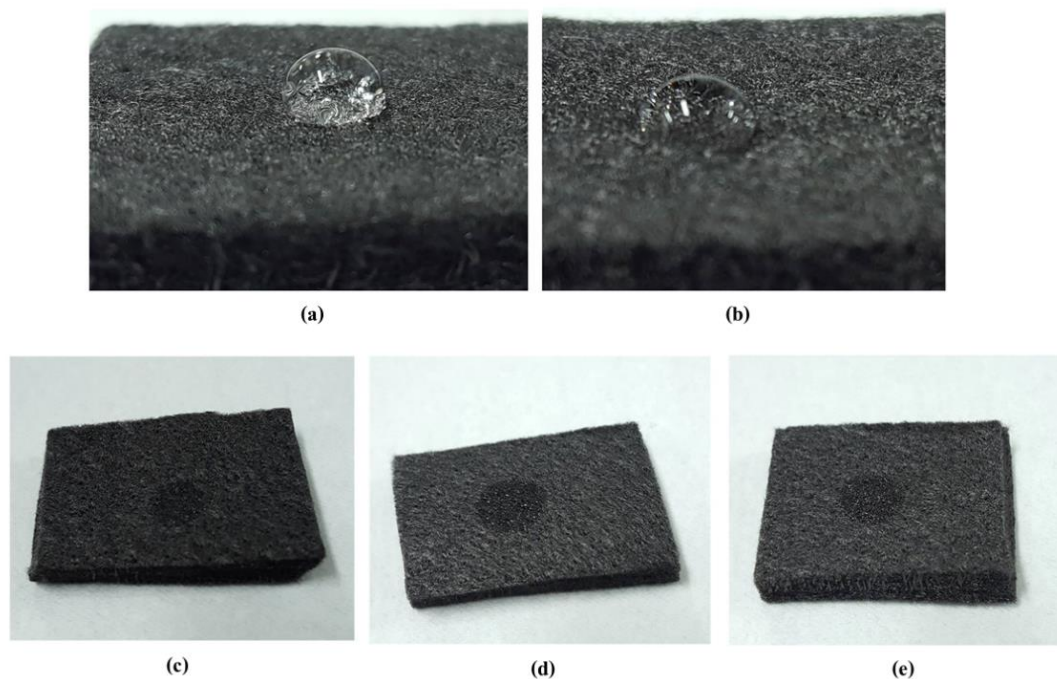
Figure 5.5 The wettability of graphite felt electrodes; (a) un-treated (b) H_2SO_4 treated (c) APPJs 450°C (d) APPJs 550°C and (e) APPJs 650°C.

5.1.2.2   The oxygen functional group on the electrode surface area

The Energy-dispersive X-ray spectroscopy (EDX) result was derived from SEM. It uses to analyze the element or chemical characteristic of a sample. Table 5.1 indicated the percentage of an oxygen atom on the electrode surface area with H_2SO_4 treated and APPJs treated which the oxygen atom of the H_2SO_4 electrode and APPJs at 550°C are the highest. Furthermore, we had analyzed the functional group on the electrode surface area by X-ray photoelectron spectroscopy (XPS) and the result shown in Table 5.2. It can see that the surface of APPJs at 550°C electrode has the highest carbonyl group (C=O) while the H_2SO_4 electrode has the lowest. The increased C=O functional group on the electrode surface cause of great the chemical activity on the electrode surface meaning the battery performance enhance (Chen et al., 2015; Li et al., 2007). Therefore, the VRFB using APPJs 550°C has the highest energy efficiency and the VRFB using H_2SO_4 is the least energy efficiency according to the performance result. On the other hand, the functional group on the surface of an

electrode treated with H_2SO_4 more transformed to the carboxyl group (O=C-O) cause EDX results shows a high amount of oxygen atom.

Table 5.1 The EDX results.

Electrode	At% of Oxygen			
	1	**2**	**3**	**Avg.**
H_2SO_4 (unused)	2.85	2.41	2.65	2.64
APPJs 450°C (unused)	1.93	0.92	1.98	1.61
APPJs 550°C (unused)	2.36	1.60	2.72	2.23
APPJs 650°C (unused)	1.88	1.71	0.96	1.52

Table 5.2 The XPS results.

Electrode	% of element				
	C-C	**C=C**	**C-O/C-N**	**C=O**	**O=C-O**
H_2SO_4	47.65	24.57	16.04	0.20	11.54
APPJ 450°C	64.67	0	22.30	7.82	5.21
APPJ 550°C	61.23	0	23.60	10.39	4.78
APPJ 650°C	61.27	0	24.48	9.00	5.25

5.2   Simulation results

5.2.1   Model validation

The reported VRFB experiment data was used to validate the developed mathematical model. The active area 10 cm^2 of a single cell VRFB with graphite felt electrode was applied. The electrode was activated by Atmospheric Pressure Plasma Jets (APPJs) at 550°C. The electrolyte solution of 50 mL in each positive and

negative reservoir was recirculated to the battery with a flow rate of 3 L/h by using two diaphragm pumps. The Nafion117 was deployed as a membrane. VRFB was operated by charging and discharging with a constant current at 0.4 A which the voltage was limited in the range of 0.7-1.7 volt. The voltage between the experiment and the simulation was different value but it was similarly curved. In this study, the charging process used the specific surface area and the standard rate constant to adjust the model parameters so that the model resembles an actual cell voltage from an experiment and the discharging process used the electrode conductivity to tune parameters together with the specific area and standard rate constant. Figure 5.6 shows the VRFB charge-discharge cell voltage of the simulation result validated with the experiment result. The simulation results explain the experimental results quite well. The maximum relative error of the cell voltage between the simulation result and the experiment result was 2.50%. This discrepancy may be caused by an imbalance of the experiment in part of the gassing side reaction occurred but the mathematical model in this study does not have the equation to explain this imbalance.

จุฬาลงกรณ์มหาวิทยาลัย

CHULALONGKORN UNIVERSITY
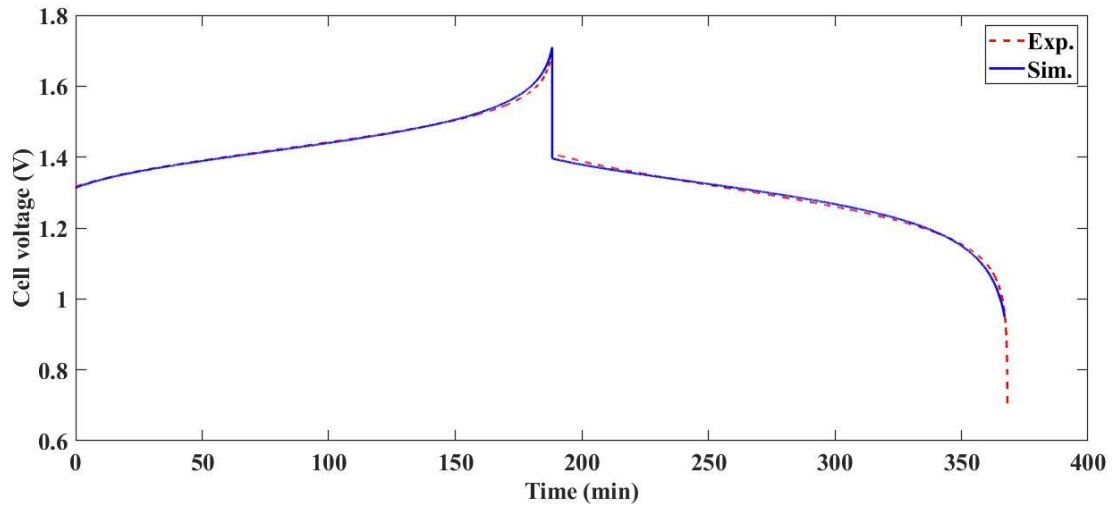
Figure 5.6 The VRFB charge-discharge cell voltage of the simulation result compared with the experiment result.

5.2.2   Artificial Neural Network results

The developed model was used to produce the input and target data that were an electrolyte flow rate, sampling time, and battery cell voltage to train Neural Network (NN) and test the performance of the trained NN model. The flow rate profile was produced by randomly in the range of 1-6 L/h at constant current density 40 mA/cm^2 under the upper and lower limit is 1.1-1.7 V, respectively.

5.2.2.1   Training result

This NN training was operated by using NARX (Nonlinear autoregressive with external input) model with 2-time delay (i-1, i-2). Trainlm (Levenberg-Marquardt backpropagation) was a training function. This architecture had two input parameters, one hidden layer, and one output parameter. The size of hidden layer was ten. Dividing the training data into 3 parts; training data 70%, validating data 15%, and testing data 15%. The charging process was trained by 15 epochs and stop training by a validation stop condition. The discharging process was trained by 35 epochs and stop training by a validation stop condition too. The

properties of the training NN were illustrated in Table 5.3 and Figure 5.7 shows the architecture of NN training.

Table 5.3 The NN training property.

Training property	Charge training	Discharge training
Architecture	2-10-1	2-10-1
Learning algorithm	Trainlm	Trainlm
Time delay	1:2	1:2
Number of nodes in hidden layer	10	10
Epochs	15	35
Training stop condition	Validation stop	Validation stop
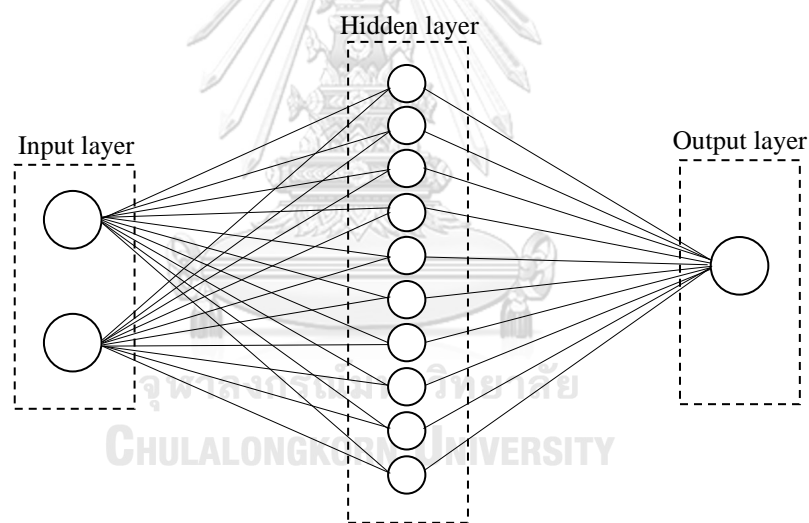
Figure 5.7 The architecture of NN training.

5.2.2.2   Testing the NN model/Prediction of NN model

Since the trained NN model may not be effective to another input data set which means when used the new input set the NN model can't accurately predict the voltage, the NN model would be necessary testing with variety input data patterns. The NN model performance testing data set was prepared several cases by the mathematical model which having different conditions such as the different constant

flow rate, the different sampling time, and the different flow rate change patterns. After the testing data collected, the pairing and sequencing follow the training set form. Figure 5.8-5.11 and Figure 5.12-5.15 show the input profile and the testing results of the charging process and discharging process, respectively. For the charging process, the testing data used different flow rate forms include constant flow, random flow, ascending flow, and descending flow as shown in Figure 5.8-5.11, respectively. Likewise, the discharging process used the testing data for different flow rate forms include constant flow, random flow, ascending flow, and descending flow as shown in Figure 5.8-5.11, respectively. The flow rates were varied from 1 to 6 L/h. From Figure 5.8-5.15, we can observe that the NN cannot predict an accurate voltage during the first period of the charging and discharging process. Since an NN model will save two last training values as i-1 and i-2 to predicting the current value (i), so the predicting value in the first period will be low efficiency.

Figure 5.8 The testing data and predicting result using the constant flow rate for charging process.
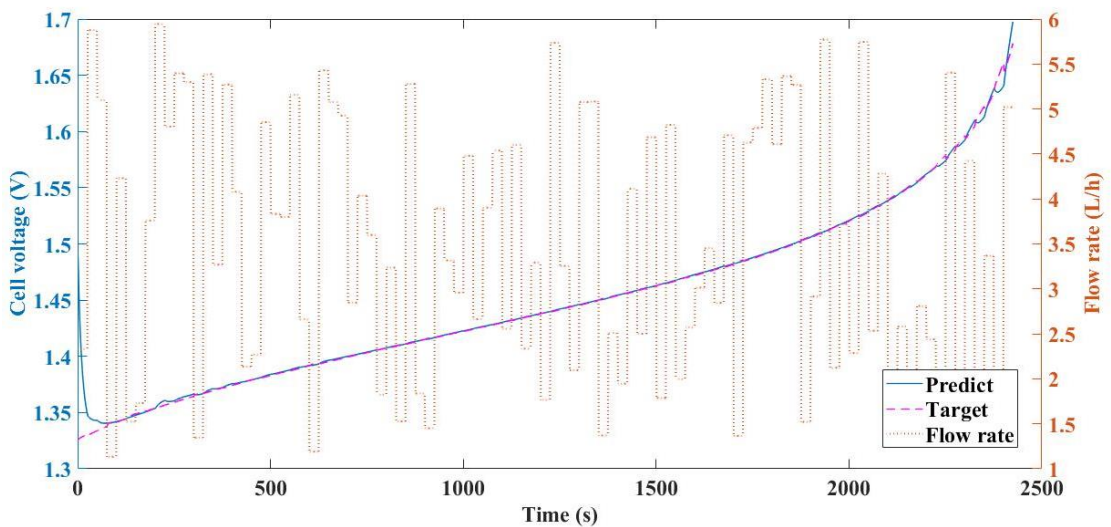
Figure 5.9 The testing data and predicting result using the random flow rate for charging process.
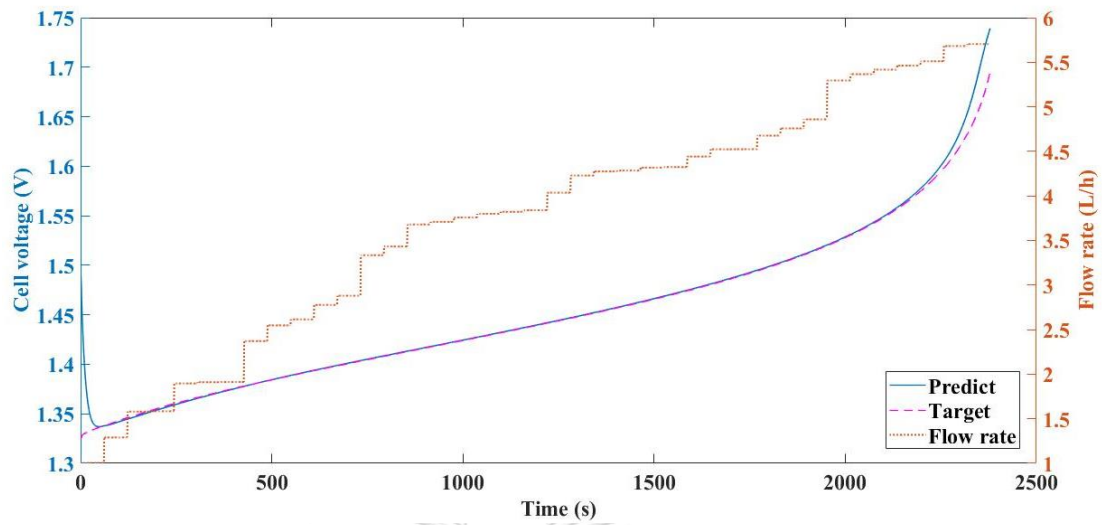
Figure 5.10 The testing data and predicting result using the ascending flow rate for charging process.
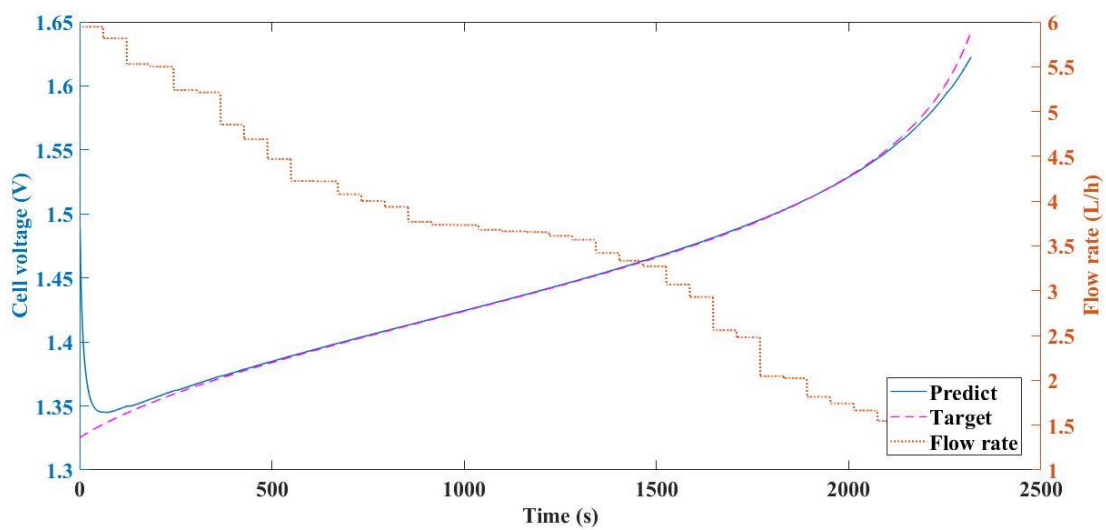
Figure 5.11 The testing data and predicting result using the descending flow rate for charging process.
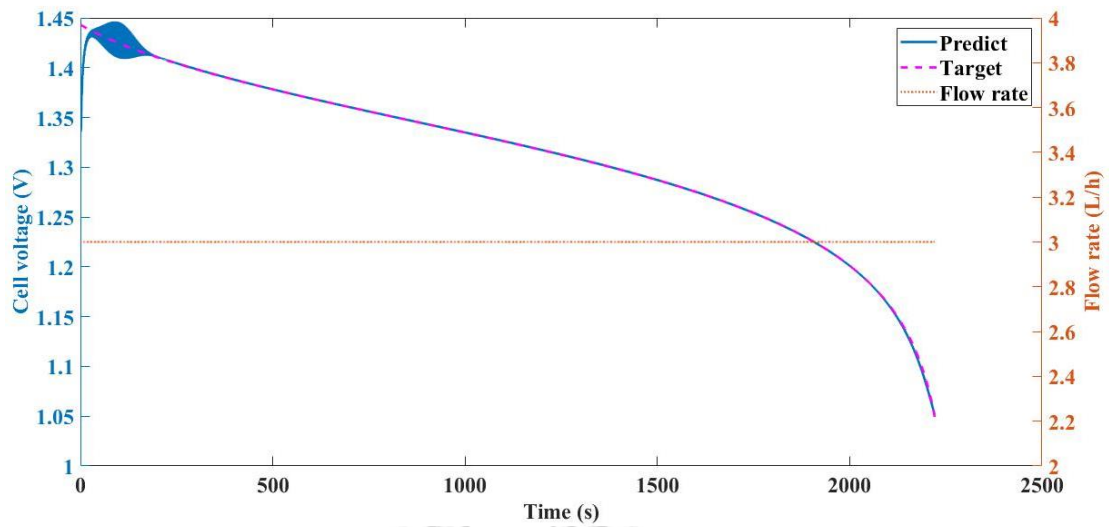
Figure 5.12 The testing data and predicting result using the constant flow rate for discharging process.
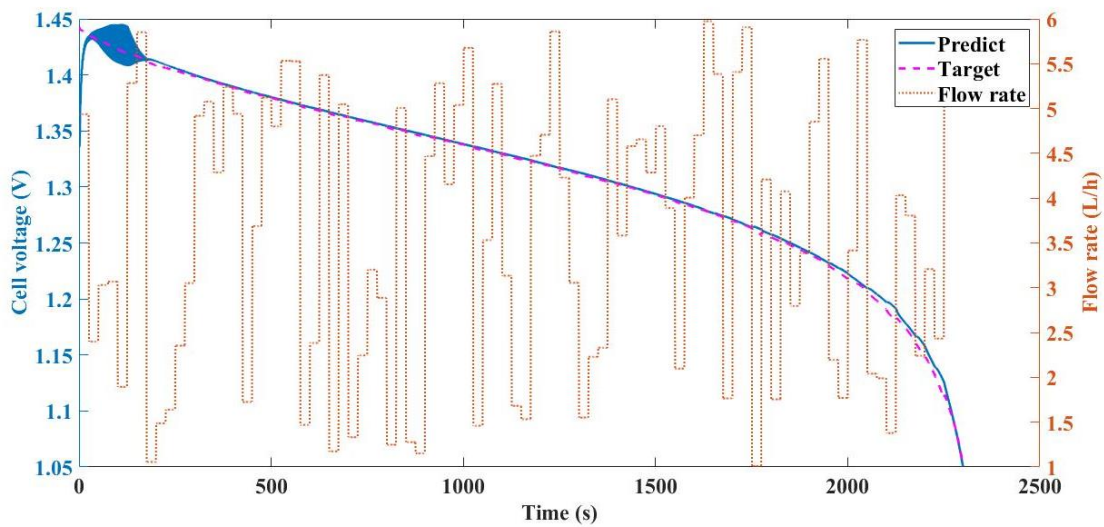
Figure 5.13 The testing data and predicting result using the random flow rate for discharging process.
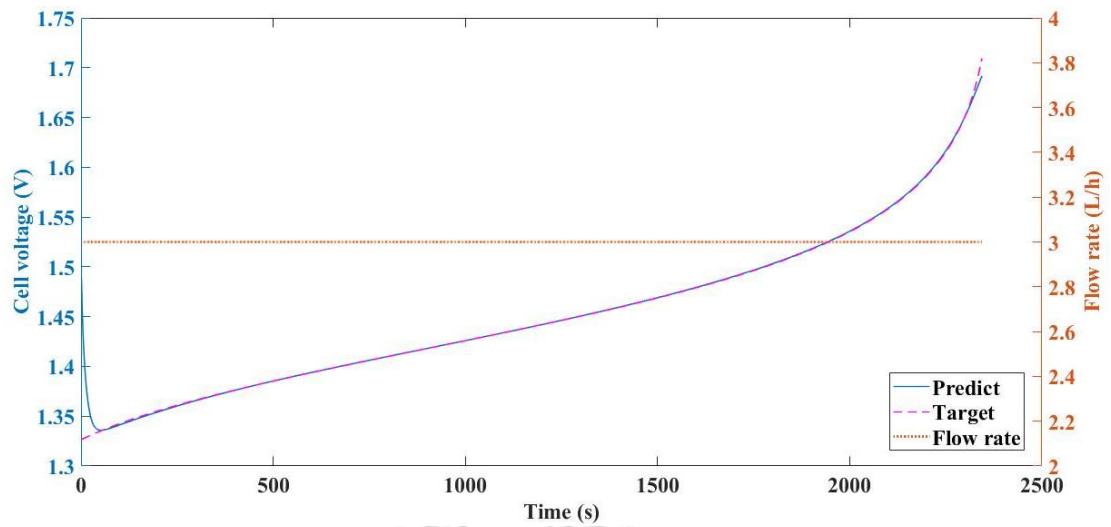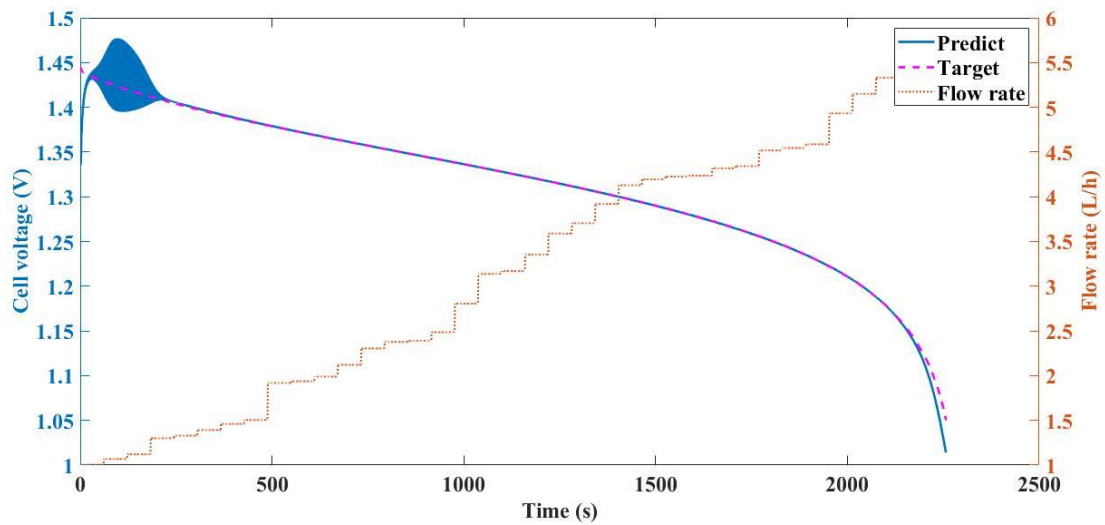
Figure 5.14 The testing data and predicting result using the ascending flow rate for discharging process.

Figure 5.15 The testing data and predicting result using the descending flow rate for discharging process.

5.2.3   Optimization based Neural Network model
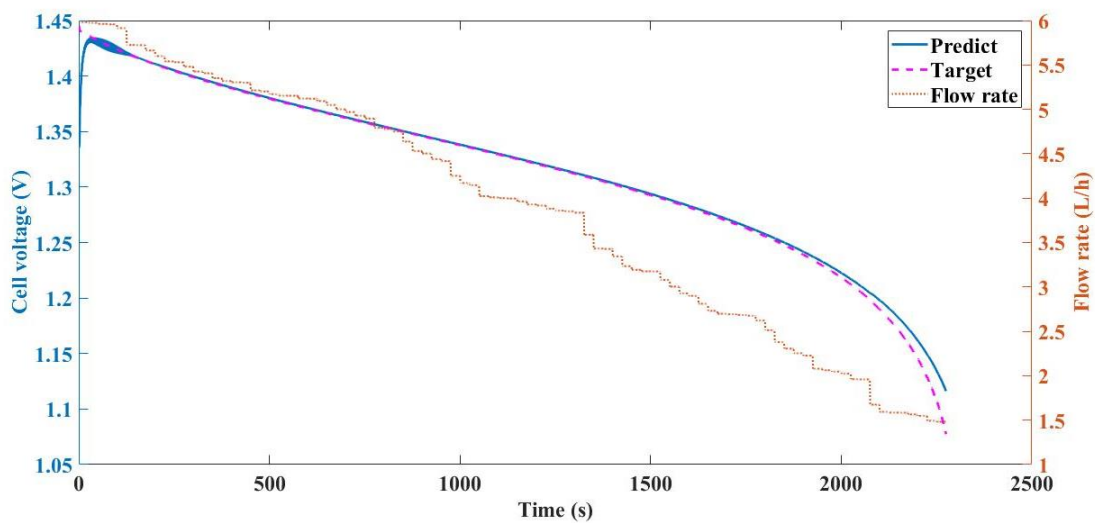
The dynamic optimization based on the Neural Network (NN) model to maximize system efficiency was performed in this study. The NN model was acted as a state predictor instead of the mathematical model to calculate or predict cell voltage

in the optimization process by using the electrolyte flow rate (Q) and stage time (t) as an input. As a reason, the optimization base on NN was comfortable to use than the optimization base on the model because the mathematical model must be specified many parameters causing the complicated.

The optimization was operated under the constant current density and constant battery temperature. The upper and lower voltage of 1.7 and 1.1 V were defined for boundary conditions. After the optimization process completely, the optimal flow rate profile was derived and carried to use in the battery that was simulated by the mathematical model. The comparison with pristine based optimization was proposed and compared the effect of optimal flow rate and constant flow rate.

Figures 5.16 and 5.17 were the optimal electrolyte flow rate from the dynamic optimization based on the mathematical model and the NN model, respectively. These optimal flow rates were similar trends. At first, the active vanadium ions in the electrolyte tanks were full, and after the charge battery, the active vanadium ions were decreased. At the early and middle process, the active vanadium ions still high causing the inflow of electrolyte into the stack each time, there will be a high amount of active species. Therefore, it was not necessary to have frequent or a large amount of electrolyte inflow to reduce the power consumption of the pump. On the other hand, the active vanadium ions concentration was decreased to a very low, electrolytes were speedy pumped into the stack to increase the recirculate of active species into the stack cause to the high energy pump consumption at the end of the process.

The dynamic optimization based on NN was compared to the dynamic optimization based on mathematical model. Figure 5.18 demonstrates the battery voltage of NN based optimization and mathematical model based. The strength blue line and the dash red line were the voltage of battery using optimal flow rate based on NN and mathematical, respectively. We observed that the NN based optimization was similarly trend to pristine based optimization. However, the optimal flow from mathematical based optimization provided the lower charging time and higher discharging time than the NN based optimization make to slightly higher system efficiency than NN. The system efficiency of NN based and mathematical based

optimization were 80.85% and 80.91%, respectively. Normally, the simulation model would have the deviation from prototype and in this study, the mathematical model was used for generating data to train the NN, thus the mathematical model was a prototype model and NN was a simulation model. As a result, an efficiency of optimal flow rate from NN based optimization was lower than mathematical model-based optimization.
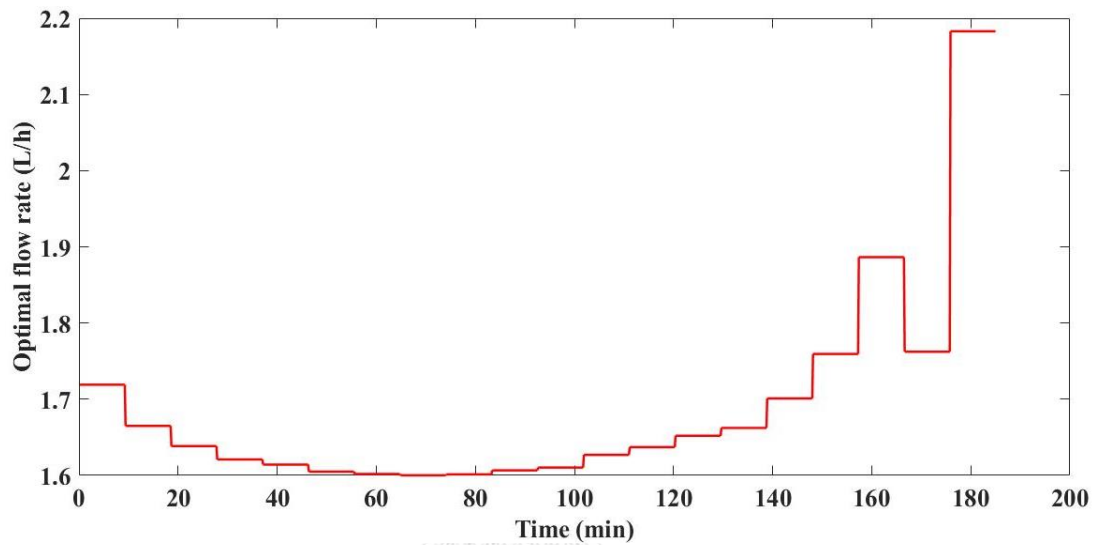
Figure 5.16 An optimal electrolyte flow rate of charging process simulated by optimization based on a mathematical model.

จุฬาลงกรณ์มหาวิทยาลัย

CHULALONGKORN UNIVERSITY
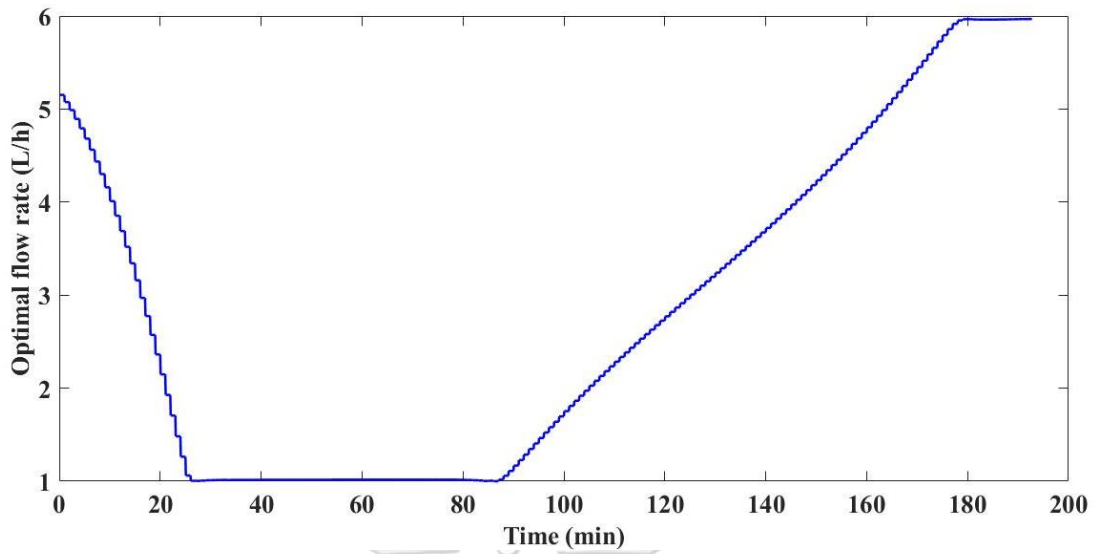
Figure 5.17 An optimal electrolyte flow rate of charging process simulated by optimization based on neural network model.
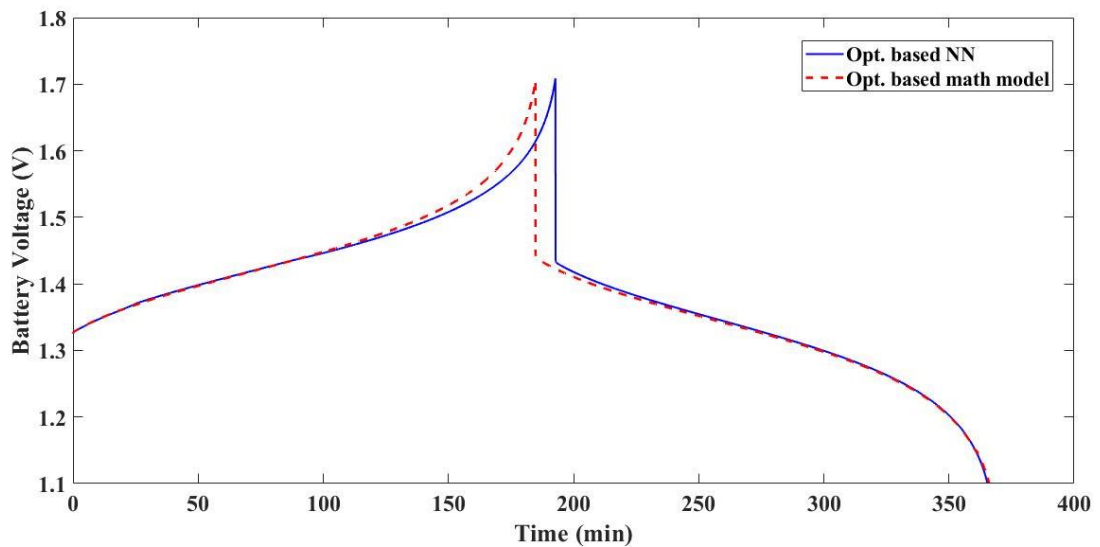
Figure 5.18 Battery voltage of the battery which uses optimal electrolyte flow rate from NN based and mathematical based optimization.

The optimal flow rate was enhancing the battery efficiency by adjustment the flow rate to suit for active species concentration for preventing the concentration loss. Especially at high state-of-charge (SOC), the active species in an electrolyte will be quite reduced thus, the electrolyte flow rate should be increased to expand opportunity

for active species flow into the cell stack and increase the quantity of active species diffuse in the active area causing to the decreased concentration overpotential. Figure 5.19 shows the concentration overpotential of battery using optimal flow rate from NN and constant flow rate at 3 L/h (the flow rate that experiment uses). We can observe that the concentration loss was constant at the early to middle SOC and rapidly rising at the end SOC. However, the concentration loss of an optimal flow rate was lower than constant flow rate which causing the increase discharge capacity.
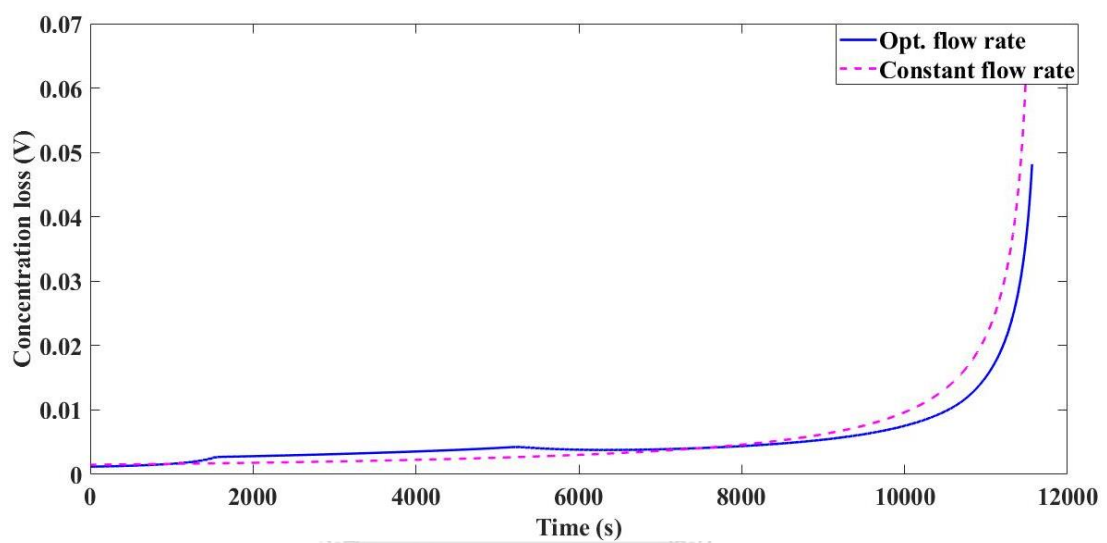
Figure 5.19 The concentration overpotential of the battery using optimal flow rate and constant flow rate.

CHAPTER 6

CONCLUSIONS AND RECOMMENDATIONS

6.1 Conclusions

The first objective of this study is to investigate the effect of the operating temperatures of the Atmospheric Pressure Plasma Jets (APPJs) process on the energy efficiency of the vanadium redox flow battery (VRFB). An experiment was operated at constant current density and electrolyte flow rate using a battery that uses graphite felt electrodes treated by APPJs with various temperatures of 450°C, 550°C, and 650°C. The electrode treated with APPJs at 550°C shows the best energy efficiency (over 83%). The characterization of the electrode was examined the Energy Dispersive X-ray Spectrometry (EDX), and the X-ray photoelectron spectroscopy (XPS). EDX showed that the APPJs electrode at 550°C has a high percentage of oxygen atom corresponding to the XPS result that showed the APPJs electrode at 550°C have the highest C=O functional group affected the highest energy efficiency. Apart from that, the effectiveness of APPJs electrode treatments was compared to untreated and sulfuric acid treatment. Although, all electrode treatments can improve the wettability, APPJs treatment method provides good performance than untreated and sulfuric acid treatment. In addition, every electrode treatment does not affect the surface of electrodes as illustrated in SEM results.

The second objective is to determine the optimal electrolyte flow rate of VRFB by solving a dynamic optimization based on a neural network model. The mathematical model was simulated and validated base on an experiment result that the battery using APPJs at 550°C treatment because it was the highest energy efficiency. The simulated battery was operated for generate data for neural network training and testing. The NN structure was two input nodes, one hidden layer with ten nodes, and one output node (2-1-1). The electrolyte flow rate and sampling time were used to input, and battery voltage was output. The NN network was structed by Nonlinear Autoregressive Exogenous (NARX) model and NN was trained by Levenberg-

Marquardt (LM) algorithm. NN was behaved to the VRFB and can predicted battery voltage accurately except the early of charge and discharge prediction. Trained NN model was used to dynamic optimization process. The optimization based on the neural network can provides higher system efficiency of vanadium redox flow battery that minimum charging power and maximum discharging power as objective functions.

6.2   Recommendations

- Since VRFB has many parameters that affect battery performance, NN could be an important role and has the ability to predict other parameters such as state-of-charge, battery temperature, and current density. Interestingly, the NN model that can be predict various parameters simultaneously.

- Normally, the current of battery operation is not stable causing some parameters are swing. The real-time optimization is a good benefit to the control system. The real-time or online optimization necessary use the online estimator, thus, the NN should be online trained.

จุฬาลงกรณ์มหาวิทยาลัย
CHULALONGKORN UNIVERSITY

REFERENCES

Abolhassani Monfared, N., Gharib, N., Moqtaderi, H., Hejabi, M., Amiri, M., Torabi, F., & Mosahebi, A. (2006). Prediction of state-of-charge effects on lead-acid battery characteristics using neural network parameter modifier. *Journal of Power Sources, 158*(2), 932-935. doi:10.1016/j.jpowsour.2005.11.023

Baral, D., Shrestha, A., Subedi, D. P., & Tyata, R. B. (2012). Development Of Atmospheric Pressure Plasma Jet In Air. *Kathmandu University Journal of Science, Engineering and Technology, 8*(1), 15-22. doi:10.3126/kuset.v8i1.6035

Bartis, E. A. J., Graves, D. B., Seog, J., & Oehrlein, G. S. (2013). Atmospheric pressure plasma treatment of lipopolysaccharide in a controlled environment. *Journal of Physics D: Applied Physics, 46*(31). doi:10.1088/0022-3727/46/31/312002

Bengui, Z., Qi, W., Shanshan, G., Zhihuan, W., Enlei, Z., Guosheng, W., . . . Shouhai, Z. (2018). High performance membranes based on new 2-adamantane containing poly(aryl ether ketone) for vanadium redox flow battery applications. *Journal of Power Sources, 399*, 18-25. doi:10.1016/j.jpowsour.2018.07.050

Binyu, X., Jiyun, Z., & Jinbin, L. (2013). Modeling of an All-Vanadium Redox Flow Battery. *IEEE*.

Bonfitto, A., Feraco, S., Tonoli, A., Amati, N., & Monti, F. (2019). Estimation Accuracy and Computational Cost Analysis of Artificial Neural Networks for State of Charge Estimation in Lithium Batteries. *Batteries, 5*(2). doi:10.3390/batteries5020047

Chang, H., Hsu, C.-M., Kao, P.-K., Yang, Y.-J., Hsu, C.-C., Cheng, I. C., & Chen, J.-Z. (2014). Dye-sensitized solar cells with nanoporous TiO2 photoanodes sintered by N2 and air atmospheric pressure plasma jets with/without air-quenching. *Journal of Power Sources, 251*, 215-221. doi:10.1016/j.jpowsour.2013.11.051

Chang, H., Yang, Y.-J., Li, H.-C., Hsu, C.-C., Cheng, I. C., & Chen, J.-Z. (2013). Preparation of nanoporous TiO2 films for DSSC application by a rapid atmospheric pressure plasma jet sintering process. *Journal of Power Sources, 234*, 16-22. doi:10.1016/j.jpowsour.2013.01.113

Chen, C. L., Yeoh, H. K., & Chakrabarti, M. H. (2014). An enhancement to Vynnycky's model for the all-vanadium redox flow battery. *Electrochimica Acta, 120*, 167-179. doi:10.1016/j.electacta.2013.12.074

Chen, J. Z., Liao, W. Y., Hsieh, W. Y., Hsu, C. C., & Chen, Y. S. (2015). All-vanadium redox flow batteries with graphite felt electrodes treated by atmospheric pressure plasma jets. *Journal of Power Sources, 274*, 894-898. doi:10.1016/j.jpowsour.2014.10.097

Chiang, M. H., Liao, K. C., Lin, I. M., Lu, C. C., Huang, H. Y., Kuo, C. L., . . . Chen, S. H. (2010). Effects of Oxygen Addition and Treating Distance on Surface Cleaning of ITO Glass by a Non-Equilibrium Nitrogen Atmospheric-Pressure Plasma Jet. *Plasma Chemistry and Plasma Processing, 30*(5), 553-563. doi:10.1007/s11090-010-9237-4

de Ramón-Fernández, A., Salar-García, M. J., Ruiz Fernández, D., Greenman, J., & Ieropoulos, I. A. (2020). Evaluation of artificial neural network algorithms for predicting the effect of the urine flow rate on the power performance of microbial fuel cells. *Energy, 213*. doi:10.1016/j.energy.2020.118806

Demuth, H., & Beale, M. (1992-2004). Neural network toolbox for use with MATLAB.

from MathWorks, Inc.

Diagram of an artificial neural network. (2013).

Dixon, D., Babu, D. J., Langner, J., Bruns, M., Pfaffmann, L., Bhaskar, A., . . . Ehrenberg, H. (2016). Effect of oxygen plasma treatment on the electrochemical performance of the rayon and polyacrylonitrile based carbon felt for the vanadium redox flow battery application. *Journal of Power Sources, 332*, 240-248. doi:10.1016/j.jpowsour.2016.09.070

Flagg, M. (2013). Structure of a Neuron. from Owlcation https://owlcation.com/stem/Structure-of-a-Neuron

Grekousis, G. (2019). Artificial neural networks and deep learning in urban geography: A systematic review and meta-analysis. *Computers, Environment and Urban Systems, 74*, 244-256. doi:10.1016/j.compenvurbsys.2018.10.008

Hasan, M. M., Ali Pourmousavi, S., Jahanbani Ardakani, A., & Saha, T. K. (2020). A data-driven approach to estimate battery cell temperature using a nonlinear autoregressive exogenous neural network model. *Journal of Energy Storage, 32*. doi:10.1016/j.est.2020.101879

Homola, T., Matoušek, J., Medvecká, V., Zahoranová, A., Kormunda, M., Kováčik, D., & Černák, M. (2012). Atmospheric pressure diffuse plasma in ambient air for ITO surface cleaning. *Applied Surface Science, 258*(18), 7135-7139. doi:10.1016/j.apsusc.2012.03.188

Hossain, M. M., Trinh, Q. H., Nguyen, D. B., Sudhakaran, M. S. P., & Mok, Y. S. (2019). Formation of plasma-polymerized superhydrophobic coating using an atmospheric-pressure plasma jet. *Thin Solid Films, 675*, 34-42. doi:10.1016/j.tsf.2019.02.017

Jirabovornwisut, T., Kheawhom, S., Chen, Y.-S., & Arpornwichanop, A. (2020). Optimal operational strategy for a vanadium redox flow battery. *Computers & Chemical Engineering, 136*. doi:10.1016/j.compchemeng.2020.106805

Kabtamu, D. M., Bayeh, A. W., Chiang, T.-C., Chang, Y.-C., Lin, G.-Y., Wondimu, T. H., . . . Wang, C.-H. (2018). TiNb2O7 nanoparticle-decorated graphite felt as a high-performance electrode for vanadium redox flow batteries. *Applied Surface Science, 462*, 73-80. doi:10.1016/j.apsusc.2018.08.101

Khamis, A., & Abdullah, S. N. S. B. (2014). Forecasting Wheat Price Using Backpropagation And NARX. *The International Journal Of Engineering And Science (IJES), 3*(11), 19-26.

Khazaeli, A., Vatani, A., Tahouni, N., & Panjeshahi, M. H. (2015). Numerical investigation and thermodynamic analysis of the effect of electrolyte flow rate on performance of all vanadium redox flow batteries. *Journal of Power Sources, 293*, 599-612. doi:10.1016/j.jpowsour.2015.05.100

Kil, D., Lee, H. J., Park, S., Kim, S., & Kim, H. (2017). Synthesis of Activated Graphite Felts Using Short-Term Ozone/Heat Treatment for Vanadium Redox Flow Batteries. *Journal of The Electrochemical Society, 164*(13), A3011-A3017. doi:10.1149/2.0311713jes

Kim, J., & Park, H. (2019). Electrokinetic parameters of a vanadium redox flow battery with varying temperature and electrolyte flow rate. *Renewable Energy, 138*, 284-291. doi:10.1016/j.renene.2019.01.102

Kim, K. J., Kim, Y.-J., Kim, J.-H., & Park, M.-S. (2011). The effects of surface modification on carbon felt electrodes for use in vanadium redox flow batteries.

Materials Chemistry and Physics, 131(1-2), 547-553. doi:10.1016/j.matchemphys.2011.10.022

Kumar, S., & Jayanti, S. (2016). Effect of flow field on the performance of an all-vanadium redox flow battery. *Journal of Power Sources, 307*, 782-787. doi:10.1016/j.jpowsour.2016.01.048

Li, X.-g., Huang, K.-l., Liu, S.-q., Tan, N., & Chen, L.-q. (2007). Characteristics of graphite felt electrode electrochemically oxidized for vanadium redox battery application. *Transactions of Nonferrous Metals Society of China, 17*(1), 195-199. doi:10.1016/s1003-6326(07)60071-5

Lim, H. S., & Kang, Y. T. (2018). Estimation of finish cooling temperature by artificial neural networks of backpropagation during accelerated control cooling process. *International Journal of Heat and Mass Transfer, 126*, 579-588. doi:10.1016/j.ijheatmasstransfer.2018.06.022

Ma, X., Zhang, H., Sun, C., Zou, Y., & Zhang, T. (2012). An optimal strategy of electrolyte flow rate for vanadium redox flow battery. *Journal of Power Sources, 203*, 153-158. doi:10.1016/j.jpowsour.2011.11.036

Materials Innovation Center, K. U. (2019). Scanning electron microscopy (SEM). Retrieved from http://mic.eng.ku.ac.th/facilities-detail.php?id_sub=42&id=39

Mjalli, F. S., Al-Asheh, S., & Alfadala, H. E. (2007). Use of artificial neural network black-box modeling for the prediction of wastewater treatment plants performance. *J Environ Manage, 83*(3), 329-338. doi:10.1016/j.jenvman.2006.03.004

Mohammadi, F., Samaei, M. R., Azhdarpoor, A., Teiri, H., Badeenezhad, A., & Rostami, S. (2019). Modelling and Optimizing Pyrene Removal from the Soil by Phytoremediation using Response Surface Methodology, Artificial Neural Networks, and Genetic Algorithm. *Chemosphere, 237*, 124486. doi:10.1016/j.chemosphere.2019.124486

Nehra, V., Kumar, A., & K Dwivedi, H. Atmospheric Non-thermal plasma sources. *International journal of engineering, 2*(1), 53-68.

Nguyen, T. D., Whitehead, A., Scherer, G. G., Wai, N., Oo, M. O., Bhattarai, A., . . . Xu, Z. J. (2016). The oxidation of organic additives in the positive vanadium electrolyte and its effect on the performance of vanadium redox flow battery. *Journal of Power Sources, 334*, 94-103. doi:10.1016/j.jpowsour.2016.10.017

Ruiz, L. G. B., Capel, M. I., & Pegalajar, M. C. (2019). Parallel memetic algorithm for training recurrent neural networks for the energy efficiency problem. *Applied Soft Computing, 76*, 356-368. doi:10.1016/j.asoc.2018.12.028

Saengrung, A., Abtahi, A., & Zilouchian, A. (2007). Neural network model for a commercial PEM fuel cell system. *Journal of Power Sources, 172*(2), 749-759. doi:10.1016/j.jpowsour.2007.05.039

Saengsawang, S. (2016). Applying for Artificial Neural Network in the Agriculture. *The Journal of King Mongkut's University of Technology North Bangkok*. doi:10.14416/j.kmutnb.2015.09.002

Schutze, A., Y. Jeong, J., E. Babayan, S., Park, J., S. Selwyn, G., & F. Hicks, R. (1998). The atmospheric-pressure plasma jet: A review and comparison to other plasma source. *IEEE Transactions on plasma science, 26*(6), 1685-1694.

Sun, B., & Skyllas-Kazacos, M. (1992a). Chemical modification of graphite electrode materials for vanadium redox flow battery application-part II Acid treatments.

Electrochimica Acta, 37(13), 2459-2465.

Sun, B., & Skyllas-Kazacos, M. (1992b). Modification of graphite electrode materials for vanadium redox flow battery application—I. Thermal treatment. *Electrochimica Acta, 37*(7), 1253-1260.

Synchrotron Thailand Central Lab, S. p. (2019). X-ray photoelectron spectroscopy (XPS). Retrieved from https://www.slri.or.th/th/index.php

Tang, A., Bao, J., & Skyllas-Kazacos, M. (2014). Studies on pressure losses and flow rate optimization in vanadium redox flow battery. *Journal of Power Sources, 248*, 154-162. doi:10.1016/j.jpowsour.2013.09.071

Tang, A., Ting, S., Bao, J., & Skyllas-Kazacos, M. (2012). Thermal modelling and simulation of the all-vanadium redox flow battery. *Journal of Power Sources, 203*, 165-176. doi:10.1016/j.jpowsour.2011.11.079

Techology, M. U. o. (2016). Artificial Neural Network. from Mahanakorn University of Techology http://www.mut.ac.th/research-detail-92

Teschke, M., Kedzierski, J., Finantu-Dinu, E. G., Korzec, D., & Engemann, J. (2005). High-speed photographs of a dielectric barrier atmospheric pressure plasma jet. *IEEE TRANSACTIONS ON PLASMA SCIENCE, 33*(2), 310-311. doi:10.1109/tps.2005.845377

The MathWorks, I. (2020). Design Time Series NARX Feedback Neural Networks. from The MathWorks, Inc. https://www.mathworks.com/help/deeplearning/ug/design-time-series-narx-feedback-neural-networks.html

Wang, T., Fu, J., Zheng, M., & Yu, Z. (2018). Dynamic control strategy for the electrolyte flow rate of vanadium redox flow batteries. *Applied Energy, 227*, 613-623. doi:10.1016/j.apenergy.2017.07.065

Wannaphong. (2016). Start Neural Networks with Python. https://python3.wannaphong.com/2016/04/neural-networks-python.html

Wu, B., Han, S., Shin, K. G., & Lu, W. (2018). Application of artificial neural networks in design of lithium-ion batteries. *Journal of Power Sources, 395*, 128-136. doi:10.1016/j.jpowsour.2018.05.040

Xu, Q., Zhao, T. S., & Leung, P. K. (2013). Numerical investigations of flow field designs for vanadium redox flow batteries. *Applied Energy, 105*, 47-56. doi:10.1016/j.apenergy.2012.12.041

Yan, Y., Li, Y., Skyllas-Kazacos, M., & Bao, J. (2016). Modelling and simulation of thermal behaviour of vanadium redox flow battery. *Journal of Power Sources, 322*, 116-128. doi:10.1016/j.jpowsour.2016.05.011

Zhang, W., Xi, J., Li, Z., Zhou, H., Liu, L., Wu, Z., & Qiu, X. (2013). Electrochemical activation of graphite felt electrode for VO2+/VO2+ redox couple application. *Electrochimica Acta, 89*, 429-435. doi:10.1016/j.electacta.2012.11.072

Zhang, X.-S. (2000). *Neural Networks in Optimization*. In. doi:10.1007/978-1-4757-3167-5

Zhao, W., Li, M.-J., Chen, X., & Tao, W.-Q. (2017). Economic analysis of a new class of vanadium redox-flow battery for medium- and large-scale energy storage in commercial applications with renewable energy. *Applied Thermal Engineering, 114*, 802-814. doi:10.1016/j.applthermaleng.2016.11.156

VITA

NAME   Apisada Chutimasakul

DATE OF BIRTH   4 August 1994

PLACE OF BIRTH   Bangkok, Thailand

INSTITUTIONS   Chulalongkorn University
ATTENDED
HOME ADDRESS   1064 Amornchai 3 village, Thawiwatthana, Bangkok,
Thailand, 10170